AGU ADVANCING EARTH AND SPACE SCIENCES

Earth and Space Science

RESEARCH ARTICLE
10.1029/2023EA003435

Ground Heat Flux Reconstruction Using Bayesian Uncertainty Quantification Machinery and Surrogate Modeling

Wenbo Zhou[1], Liujing Zhang[1], Aleksey Sheshukov[2], Jingfeng Wang[3], Modi Zhu[3], Khachik Sargsyan[4], Donghui Xu[5], Desheng Liu[6], Tianqi Zhang[6], Valeriy Mazepa[7], Alexandr Sokolov[8], Victor Valdayskikh[9], and Valeriy Ivanov[1]

[1]Department of Civil and Environmental Engineering, University of Michigan, Ann Arbor, MI, USA, [2]Department of Biological and Agricultural Engineering, Kansas State University, Manhattan, KS, USA, [3]School of Civil and Environmental Engineering, Georgia Institute of Technology, Atlanta, GA, USA, [4]Sandia National Laboratories, Livermore, CA, USA, [5]Pacific Northwest National Laboratory, Richland, WA, USA, [6]Department of Geography, Ohio State University, Columbus, OH, USA, [7]Institute of Plant and Animal Ecology, the Ural Branch of the Russian Academy of Sciences, Yekaterinburg, Russia, [8]Arctic Research Station, Institute of Plant and Animal Ecology, the Ural Branch of the Russian Academy of Sciences, Labytnangi, Russia, [9]Ural Federal University, Yekaterinburg, Russia

Abstract Ground heat flux (G_0) is a key component of the land-surface energy balance of high-latitude regions. Despite its crucial role in controlling permafrost degradation due to global warming, G_0 is sparsely measured and not well represented in the outputs of global scale model simulation. In this study, an analytical heat transfer model is tested to reconstruct G_0 across seasons using soil temperature series from field measurements, Global Climate Model, and climate reanalysis outputs. The probability density functions of ground heat flux and of model parameters are inferred using available G_0 data (measured or modeled) for snow-free period as a reference. When observed G_0 is not available, a numerical model is applied using estimates of surface heat flux (dependent on parameters) as the top boundary condition. These estimates (and thus the corresponding parameters) are verified by comparing the distributions of simulated and measured soil temperature at several depths. Aided by state-of-the-art uncertainty quantification methods, the developed G_0 reconstruction approach provides novel means for assessing the probabilistic structure of the ground heat flux for regional permafrost change studies.

Plain Language Summary Ground heat flux is the energy that goes into or comes out from belowground that controls the soil freeze-thaw process in high-latitude regions. Its changes under climate warming will influence variations in the soil's seasonal thawing depth and permafrost thickness and spatial extent. Available data on ground heat flux are very sparse from both direct field measurements and large-scale model outputs in the Arctic. This study combines detailed modeling and uncertainty quantification methods to accurately reconstruct the ground heat flux from shallow soil temperature observations and estimates from predictive models, which are more readily available for the Arctic. Since the approach relies on several assumptions, we also quantify the uncertainty of the estimated ground heat flux. The reconstructed ground heat fluxes using the method developed in this study match well with the fluxes observed or derived from the predictive model. The soil properties inferred from the developed process are also consistent with the values observed for typical soils.

Key Points:

- Ground heat flux is reconstructed from various types of shallow soil temperature and auxiliary data using an analytical heat transfer model
- Uncertainty quantification methods are applied to infer model parameters and increase simulation efficiency drastically
- The efficacy of the proposed ground heat flux reconstruction framework is shown by agreement between simulation and observation

Supporting Information:

Supporting Information may be found in the online version of this article.

Correspondence to:

V. Ivanov,
ivanov@umich.edu

Citation:

Zhou, W., Zhang, L., Sheshukov, A., Wang, J., Zhu, M., Sargsyan, K., et al. (2024). Ground heat flux reconstruction using Bayesian uncertainty quantification machinery and surrogate modeling. *Earth and Space Science*, *11*, e2023EA003435. https://doi.org/10.1029/2023EA003435

Received 16 NOV 2023
Accepted 8 FEB 2024

Author Contributions:

Conceptualization: Wenbo Zhou, Valeriy Ivanov
Data curation: Wenbo Zhou, Modi Zhu, Victor Valdayskikh
Formal analysis: Wenbo Zhou, Liujing Zhang
Funding acquisition: Aleksey Sheshukov, Jingfeng Wang, Desheng Liu, Valeriy Mazepa, Victor Valdayskikh, Valeriy Ivanov
Methodology: Wenbo Zhou, Aleksey Sheshukov, Jingfeng Wang,

1. Introduction

Ground heat flux (G_0) is defined as the diffusive heat flow across the boundary that separates the bottom of the atmosphere and the ground. It is a crucial component of the land surface energy balance, especially in the high-latitude regions as the driver of water phase change (El Sharif et al., 2019; Halliwell & Rouse, 1987; Lunardini, 1981; Ochsner & Baker, 2008). G_0 controls the dynamics of freeze and thaw and permafrost degradation in Arctic regions (Biskaborn et al., 2019). However, the quantification of G_0 has received less attention in the past (Heusinkveld et al., 2004; Wu et al., 2020) and the impact of climate change on G_0 is not well understood (e.g., Nicolsky & Romanovsky, 2018).

Direct measurement of G_0 can be made using heat flux plates (e.g., HukseefluxUSA Inc. HFP01 Heat Flux Sensor) buried at shallow depths in the soil to ensure a tight contact between the plate surface and soil substrate (surficial

Modi Zhu, Khachik Sargsyan, Donghui Xu, Valeriy Ivanov
Resources: Alexandr Sokolov, Victor Valdayskikh
Supervision: Aleksey Sheshukov, Jingfeng Wang, Valeriy Ivanov
Validation: Wenbo Zhou, Liujing Zhang, Aleksey Sheshukov, Jingfeng Wang, Khachik Sargsyan, Donghui Xu, Desheng Liu, Tianqi Zhang, Valeriy Mazepa, Alexandr Sokolov, Victor Valdayskikh, Valeriy Ivanov
Visualization: Wenbo Zhou
Writing – original draft: Wenbo Zhou
Writing – review & editing: Wenbo Zhou, Aleksey Sheshukov, Jingfeng Wang, Modi Zhu, Khachik Sargsyan, Donghui Xu, Desheng Liu, Tianqi Zhang, Valeriy Mazepa, Alexandr Sokolov, Victor Valdayskikh, Valeriy Ivanov

deployment is impossible due to the disturbances by radiation and precipitation) and combined with soil temperature measurements in the layer above the plate (El Sharif et al., 2019). However, such measurements are extremely sparse in remote Arctic regions because they are costly and logistically challenging. Large-scale data products from Global Climate Models (GCMs) are often used to project permafrost thermal states into the future under different climate scenarios. However, they usually do not provide direct outputs of G_0 for either historical or future periods. Instead, G_0 needs to be derived as the residual term of the surface energy balance equation when the data on net radiation (R_n), sensible (H), and latent (λE) heat flux are available. This approach is only applicable to snow-free surfaces. For snow covered surfaces, the change in the internal energy of the snowpack (heat associated with heating/cooling and water phase change) is required to derive G_0. Yet, the internal energy change of snowpack is usually not an explicit output of most GCMs. This situation also pertains for climate reanalysis data products.

Several analytical methods have been developed to derive G_0. Traditional methods for modeling G_0 require multi-depth data of soil temperature with soil properties such as bulk density, specific heat and thermal conductivity (Cobos & Baker, 2003; Fuchs & Tanner, 1968a; Horton & Wierenga, 1983; Kimball et al., 1976; Ochsner & Baker, 2008; Ochsner et al., 2006). For the case of homogeneous soils without water phase change, an analytical solution of soil heat flux and temperature at any depth can be derived from a harmonic analysis using measured soil temperature (Heusinkveld et al., 2004). However, its accuracy decreases with measurement depth. Under the same assumptions of homogeneity and water state condition for a semi-infinite soil column, an analytical solution of G_0 can be derived assuming sinusoidal surface temperature boundary condition (Gao et al., 2010). Analogously, G_0 can also be derived from the Green's function solution (Wang & Bou-Zeid, 2012) or from the soil heat flux at a deeper depth through "damping depth" (Leuning et al., 2012). Wang and Bras (1999) developed an analytical relationship between soil temperature and ground heat flux at the same depth through a half-order derivative (HOD) method (see Sec. 2.1.1 for details). Using this analytical solution (referred to as the HOD model hereafter), G_0 can then be derived from surface temperature time series given the thermal inertia of the bulk soil. In general, all analytical solutions require surface soil temperature as input.

Surface temperature measurements using ground-based instruments are difficult to obtain and not commonly available in the Arctic regions. For example, measurements using thermometers are subject to substantial sampling errors caused by poor contact between the sensor and the surface and the disturbances from direct sunlight and diffuse sky radiation (Fuchs & Tanner, 1968b). The measurements of contactless infrared temperature sensors are affected by calibration errors and other technical problems such as optical path blocking by snowflakes or vegetation elements (Apogee Instruments, 2018). For monitoring the subsurface conditions, temperature sensors are usually placed at some depths below ground, for example, in narrow and deep boreholes, which provides long-term time series of multi-level soil temperatures in the Arctic regions. However, existing analytical solutions such as the HOD model cannot be used to *directly* derive surface ground heat flux from belowground borehole temperature measurements. This is because the nonexistence of the inverse Laplace transform in the formula derivation and the divergence of the inverse estimation.

Soil thermal properties such as thermal inertia and thermal diffusivity need to be specified in model formulation (e.g., the HOD model). These model parameters can be a priori determined from a given soil composition, that is, soil texture, soil organic material content, and soil water content (Farouki, 1981; Johansen, 1977; Lawrence & Slater, 2007). The measurements of soil texture needed to derive such thermal properties are still lacking in the Arctic, and due to the intrinsic environmental heterogeneity and small-scale nature of their sampling (e.g., "fist-size" auger soil samples), they can be extremely noisy. Efforts have been made in previous studies to estimate soil thermal properties from soil temperature series. For example, Nicolsky et al. (2009) have applied the Quasi-Newton optimization algorithm to find the optimal parameters that minimize the mismatch between modeled and measured soil temperature (or "cost function"). However, such an approach requires a proper initial guess of the soil properties that make the cost function in the attraction basin of its global minimum to ensure efficient convergence. Besides using optimization methods to calibrate model parameters for soil properties, parameter uncertainties are usually characterized by using probabilistic methods. Garnello et al. (2021) and Harp et al. (2016) have used the Markov Chain Monte Carlo (MCMC) and null-space Monte Carlo (NSMC) respectively to estimate parameter posterior distribution. However, in both studies, forward model results are directly used in the calibration process or in the likelihood function, which can be computationally costly for complex models. Cleary et al. (2021) and Groenke et al. (2022) have applied the ensemble Kalman sampling (EKS) algorithm to generate approximate samples from the parameter posterior. The EKS method requires a multivariate

Gaussian prior distribution over parameters (which may not usually be the case) and will underestimate posterior variance with finite algorithm iterations. This raises a question: can effective magnitudes of soil thermal properties be evaluated automatically and efficiently using only soil temperature measurements? Furthermore, considering the close correlation between heat flux and temperature, if the effective soil properties can be inversely inferred from observed physical states (such as soil temperature), can ground heat flux be reconstructed with its uncertainty quantified?

The goal of this research is the development and demonstration of the efficacy and uncertainty-informed accuracy of a novel methodological approach for estimating the surface ground heat flux over different seasons from soil temperature and soil moisture series (if available) measured at a range of depths below the ground surface. Three methodological "blocks" are used to achieve this goal. The analytical HOD model is used to derive ground heat flux from soil temperature (and moisture if available). A physically based numerical model (Sheshukov & Egorov, 2002) is used to simulate non-isothermal heat-moisture dynamics and the resultant temperature and water phase series from the surface flux G_0. Finally, modern advancements in probabilistic learning and uncertainty quantification (UQ) machinery (Dwelle et al., 2019; Ghanem et al., 2017; Sraj et al., 2014) are used to derive the probabilistic description of soil thermal properties used in the analytical and numerical model. Specifically, the more complex analytical and numerical models are first mimicked by a less complex surrogate model built from polynomial chaos expansion to increase computation speed. Model parameters are then estimated using the Bayesian inference framework. The Karhunen-Loève expansion, which is not yet widely used in geoscience and cryosphere studies (e.g., Dong et al., 2006; Rundle et al., 2000; Tiampo et al., 2004), is applied to reduce spatiotemporal dimensionality of model outputs and improve the parameter inference efficiency. Accurate field measurements of G_0 series or estimates obtained from global scale model outputs during snow-free seasons are used as the "ground-truth" reference for parameter inference procedure. In the more typical case when G_0 data are not available, temperature series at different depths of the soil column (such as in a borehole) are used to estimate flux G_0, which is subsequently verified by comparing the simulations of soil temperature from a physically based numerical model with temperature measurements.

2. Methods

2.1. HOD Solution of Ground Heat Flux and Soil Temperature

2.1.1. Analytical Model Formulation

The HOD model formulation is briefly described here and a full description is in Wang and Bras (1999). For a one-dimensional semi-infinite soil column, the heat transfer process follows the classical thermal diffusion equation with no phase change that assumes constant thermal diffusivity and a uniform initial temperature profile. Ground heat flux at depth z_2 ($G(z_2, t)$) can be derived from soil temperature at depth z_1 ($T(z_1, t)$),

$$G(z_2, t) = \frac{I}{\sqrt{\pi}} \int_0^t \exp\left[-\frac{(z_2 - z_1)^2}{4D(t-\tau)}\right] \frac{dT(z_1,\tau)}{\sqrt{t-\tau}} \tag{1}$$

where I is the soil thermal inertia ($W^2\ s\ m^{-4}\ K^{-2}$), D is the soil thermal diffusivity ($m^2\ s^{-1}$), t is time (s), and τ is the integration dummy variable. With positive direction for depth defined downward from the surface, this solution requires $0 \le z_1 \le z_2$. The equality $\tau = 0$ in Equation 1 is set at the time when G_0 is as close to zero as possible. Soil thermal inertia, I, is defined as

$$I = \sqrt{kc_v}, \tag{2}$$

and soil thermal diffusivity, D, is defined as

$$D = \frac{k}{c_v}, \tag{3}$$

where k is the soil thermal conductivity ($W\ m^{-1}\ K^{-1}$), and c_v is the soil volumetric heat capacity ($J\ m^{-3}\ K^{-1}$).

2.1.2. Parameter Separation

Thermal properties of the soil are affected by its water content, in liquid or solid phase. In the original formulation of the HOD model, thermal inertia is assumed to be time invariant. In practice, it varies with water content and phase over seasonal scale. The top soil layer in the Arctic, known as the active layer, also undergoes seasonal thawing and freezing cycles. The mineral soil in the active layer is usually near saturation for much of the year and may become unsaturated during summer, while the shallow layer of well-drained and organic-rich soil at the top of the active layer may be desiccated even in winter (Hinkel et al., 2001; Hinzman et al., 1991; Kane et al., 1989). The effects of soil water content and phase change on the thermal inertia value are accounted for by separating the parameters previously considered as time-invariant into time-dependent and temporally constant parts.

Following a linear mixing model, soil thermal conductivity k and volumetric heat capacity c_v are computed using the set of equations as in Lawrence and Slater (2007). For soil thermal conductivity:

$$k = K_e k_{sat} + (1 - K_e) k_{dry}, \tag{4}$$

$$K_e = \begin{cases} \log S_r + 1, & T \geq T_f \\ S_r, & T < T_f \end{cases}, \tag{5}$$

$$k_{sat} = k_s^{1-\theta_{sat}} k_{liq}^{\frac{\theta_{liq}}{\theta_{liq}+\theta_{ice}}\theta_{sat}} k_{ice}^{\left(1-\frac{\theta_{liq}}{\theta_{liq}+\theta_{ice}}\right)\theta_{sat}}, \tag{6}$$

$$S_r = \frac{\theta_{liq} + \theta_{ice}}{\phi} \approx \frac{\theta_{liq} + \theta_{ice}}{\theta_{sat}}, \tag{7}$$

For soil volumetric heat capacity:

$$c_v = c_h + \theta_{liq} c_{liq} + \theta_{ice} c_{ice}, \tag{8}$$

Names and units of the parameters in Equations 4–8 are listed in Table 1. The parameters k_{liq}, k_{ice}, c_{liq}, and c_{ice} are treated as constants. The variable θ_{sat} is determined by finding the maximum value in the observed series of $\theta_{liq} + \theta_{ice}$ and assumed to be equal to porosity, that is, $\phi \approx \theta_{sat} \approx \theta_{liq} + \theta_{ice}$. Three time-invariant parameters can be identified from these equations: c_h, k_{dry}, and k_s. Other parameters are time-varying and dependent on the temporal evolution of soil liquid water and ice content. After soil thermal properties are computed using available records of soil water content and the time-invariant properties are determined in any appropriate fashion (e.g., literature values, measurement of in situ sample, or model parameter inference), ground heat flux can then be calculated using these derived soil thermal properties and the HOD model.

2.2. 1-D Freeze-Thaw Numerical Model for Saturated Soil

The simulation of soil freezing and thawing processes is an active research topic for cold climate region due to their important roles in climate change, active layer and permafrost depths, hydrologic regimes, and cold region infrastructure sustainability (Hjort et al., 2022; Matzner & Borken, 2008; Painter et al., 2012, 2016; Walvoord & Kurylyk, 2016). Various numerical models were developed to solve the coupled heat and moisture dynamics of frozen soil (Harlan, 1973; Mu & Ladanyi, 1987; Painter & Karra, 2014; Sheshukov & Nieber, 2011; Taylor & Luthin, 1978; Tubini et al., 2021; Westermann et al., 2016, 2023; Zhang et al., 2007). In this study, we adopt the solution for the saturated frozen soil from Sheshukov and Egorov (2002).

The one-dimensional (1-D) equation of heat transfer in soils is:

$$\frac{\partial}{\partial t}\left(c_v T - \rho_i \phi L_f S_i\right) = \frac{\partial}{\partial z}\left(k \frac{\partial T}{\partial z}\right), \tag{9}$$

where the variables are defined in Table 1. The advective heat flux associated with bulk movement of water in the soil in Sheshukov and Egorov's (2002) original formulation is neglected here considering that the heat transfer is

Table 1
Nomenclature

Parameter	Name	Unit	Model[a]
k_{dry}	Dry soil thermal conductivity	W m^{-1} K^{-1}	A
k_{sat}	Saturated soil thermal conductivity	W m^{-1} K^{-1}	A
K_e	Kersten number (the weight for k_{sat} in Equation 4 for soil thermal conductivity calculation)	–	A
S_r	Degree of saturation for total water content	–	A
$T_f = 273.15$	Freezing temperature of water	K	A, N
k_s	Soil solid thermal conductivity	W m^{-1} K^{-1}	A
θ_{sat}	Saturated volumetric water content	–	A
θ_{liq}	Liquid water content	–	A
θ_{ice}	Ice content	–	A
$k_{liq} = 0.57$	Thermal conductivity of liquid water	W m^{-1} K^{-1}	A
$k_{ice} = 2.3$	thermal conductivity of ice	W m^{-1} K^{-1}	A
c_h	Volumetric heat capacity of soil constituents excluding water and ice	J m^{-3} K^{-1}	A
$c_{liq} = 4.2 \times 10^6$	Volumetric heat capacity of liquid water	J m^{-3} K^{-1}	A
$c_{ice} = 2.0 \times 10^6$	Volumetric heat capacity of ice	J m^{-3} K^{-1}	A
ϕ	Porosity	-	A, N
$\rho_i = 918.0$	Density of ice	kg m^{-3}	N
$\rho_w = 1{,}000.0$	Density of liquid water	kg m^{-3}	N
$L_f = 3.34 \times 10^5$	Latent heat of freezing for water	J kg^{-1}	N
S_i	Degree of saturation for ice	–	N
S_w	Degree of saturation for liquid water	–	N
b	Reciprocal of pore size distribution index in the B-C model	–	N
ψ_s	Air entry pressure head in the B-C model	m	N
$g = 9.8$	Gravitational acceleration	m s^{-2}	N
$\tilde{G}_0$	Approximate ground heat flux at the surface, scaled from HOD model results at shallow depth	W s^{-2}	A
G_0^{FS}	Measured ground heat flux at the surface including energy storage correction (Sec. 3.1)	W s^{-2}	–
G_0^{GCM}	Ground heat flux derived by Equation 25, using GCM data product	W s^{-2}	–
G_0^{ERA5}	Ground heat flux derived by Equation 25, using ERA5-Land reanalysis data product	W s^{-2}	–
z_i	The i-th observation depth	m	–
T_i	Measured temperature at the depth of z_i	°C	–

[a]A: analytical model. N: numerical model.

dominated by conduction, and phase change as water in the soil is nearly immobile. Under the fully saturated condition,

$$S_w + S_i = 1. \tag{10}$$

When soil temperature T is above the freezing point of water T_f, $S_w = 1$ and $S_i = 0$.

The freezing-thawing phenomena is considered to be similar to the drying-wetting phenomena (Koopmans & Miller, 1966) for which liquid water pressure head (ψ_w) and ice pressure head (ψ_i) and relative saturation S_w are described by a water retention function $P_c(S_w)$ adopted from the Brooks and Corey (B-C) model (Brooks & Corey, 1966):

$$\psi_w - \psi_i = \gamma P_c(S_w) = \gamma \psi_s {S_w}^{-b}. \tag{11}$$

Assuming no frost heave presence, ψ_i is set to be zero in this study. The coefficient γ is the ratio of specific surface energies at the ice-water interfaces (Koopmans & Miller, 1966) depending on soil saturation condition and soil texture and set to 1.0 in this study. Assuming equilibrium at the ice-water interface, the generalized Clapeyron equation (Miller, 1980) is:

$$\frac{\psi_w}{\rho_w} - \frac{\psi_i}{\rho_i} = \frac{L_f}{\rho_w g T_f} T. \tag{12}$$

Under specific boundary and initial condition, the temperature and moisture profile of the soil column can be solved simultaneously from Equations 9–12. A detailed model setup example is presented in Supporting Information S1 (Text S3). For the scope of this study, the frozen soil is considered as porous media without fracture, its deformation and cryosection effects are currently not considered. Uncertainties arise with this adapted model when the assumptions of restricted parameter settings (e.g., $\psi_i = 0$, $\gamma = 1.0$) and full saturation are applied. However, using the parameter inference process with the embedded uncertainty quantification machinery, as described below, these uncertainties are implicitly included in the inferred parameter distributions.

2.3. UQ Machinery

Mechanistic models including the HOD model are developed based on physical principles with certain assumptions and approximations to describe the behavior of physical systems. Both model inputs (spatial or temporal fields of states) and the parameters (e.g., proxies or intrinsic medium properties) have uncertainties. Probabilistic methods have been widely used to quantify the uncertainty and infer values for model parameters (Dwelle et al., 2019; Ellison, 2004; Malinverno, 2002; Sargsyan et al., 2014, 2015; Sraj et al., 2014). In this section, UQ methodological steps are briefly introduced and an overview of the workflow is described.

2.3.1. Bayesian Inference

We define a "forward problem" as the simulation of quantities of interest (QoIs) using a mechanistic model M with prescribed model parameter set $\boldsymbol{\kappa} = (\kappa_1, \kappa_2, \ldots, \kappa_m)$, where m is the number of parameters in M. Similarly, an "inverse problem" can be formulated as follows: given available observations on QoIs and a set of modeled results using the uncertain parameters $\boldsymbol{\kappa}$, can one infer the *most likely* values in the parameter set $\boldsymbol{\kappa}$, to achieve a minimum discrepancy between the simulated QoIs with observations?

Bayesian inference is a widely used approach to solve such inverse problems (e.g., Dwelle et al., 2019; Hou & Rubin, 2005; Sargsyan et al., 2015; Sraj et al., 2014; Tarantola, 2005). In general, let $\boldsymbol{Y} = (Y_1, \ldots, Y_Q)$ be a vector of available QoI data, and $\boldsymbol{\kappa}$ be the vector of uncertain model parameters. Then modeled outputs can be assumed to represent the QoI data:

$$\boldsymbol{Y} \approx M(\boldsymbol{\kappa}). \tag{13}$$

The cornerstone of the Bayesian inference of model parameters is the Bayes' theorem which in this context reads as:

$$\Pi(\boldsymbol{\kappa}|\boldsymbol{Y}) \propto L(\boldsymbol{Y}|\boldsymbol{\kappa})\, p(\boldsymbol{\kappa}), \tag{14}$$

where $p(\boldsymbol{\kappa})$ is the prior distribution of the set $\boldsymbol{\kappa}$ constructed from a priori information about the parameters (see Text S1 in Supporting Information S1); $L(\boldsymbol{Y}|\boldsymbol{\kappa})$ is the likelihood function quantifying the probability of producing observations on the QoIs by M given the set $\boldsymbol{\kappa}$. The likelihood function encapsulates the assumptions about the distribution of discrepancy between model and data. Assuming that each component of the discrepancy between observed data Y_i and modeled results $M_i(\boldsymbol{\kappa})$, that is, $\epsilon_i = Y_i - M_i(\boldsymbol{\kappa})$, adheres to a probability density function p_{ϵ_i}, and observational data are independent and identically distributed, one can write the likelihood as:

$$L(\boldsymbol{Y}|\boldsymbol{\kappa}) = \prod_{i=1}^{Q} p_{\epsilon_i}(Y_i - M_i(\boldsymbol{\kappa})). \tag{15}$$

Furthermore, we assume that the errors ϵ_i follow Gaussian distribution $\epsilon_i \sim N\left(0, {\sigma_i}^2\right)$, leading to a likelihood function:

$$L(\boldsymbol{Y}|\boldsymbol{\kappa}) = \prod_{i=1}^{Q} \frac{1}{\sqrt{2\pi{\sigma_i}^2}} \exp\left(-\frac{(Y_i - M_i(\boldsymbol{\kappa}))^2}{2{\sigma_i}^2}\right), \tag{16}$$

where ${\sigma_i}^2$ is the variance of the QoI observational data noise.

Finally, assuming independent prior distributions, the final joint posterior distribution can be written as:

$$\Pi(\boldsymbol{\kappa}|\boldsymbol{Y}) \propto \prod_{i=1}^{Q} \frac{1}{\sqrt{2\pi{\sigma_i}^2}} \exp\left(-\frac{(Y_i - M_i(\boldsymbol{\kappa}))^2}{2{\sigma_i}^2}\right) p(\kappa_1)\, p(\kappa_2) \ldots p(\kappa_m), \tag{17}$$

Note that Equation 17 is the posterior distribution up to a constant factor. The full joint posterior distribution is typically unavailable in closed form, and therefore we resort to Markov Chain Monte Carlo (MCMC) method using the Metropolis–Hastings algorithm (Hastings, 1970) that produces samples of the posterior distribution. We used adaptive MCMC (Haario et al., 2001) that efficiently explores the parameter space by adaptively updating MCMC proposal covariance. Specifically, MCMC samples are filtered by removing the first 25% values of the MCMC parameter sequence and choosing every fifth value in the remaining set to reduce correlations in the chain. This reduced set of posterior parameter values is then used to evaluate full distribution or its marginals using kernel density estimation (KDE).

2.3.2. Surrogate Modeling

The formulation above assumes a vector of QoIs $\boldsymbol{Y} = (Y_1, \ldots, Y_Q)$ and associated vector of model outputs $M_i(\boldsymbol{\kappa})$, for $i = 1, 2, \ldots, Q$. The sampling process in Sec. 2.3.1 requires repeated simulations of the mechanistic model M for computing the likelihood function, which is computationally expensive. A feasible technique to improve computational efficiency is to replace the mechanistic model with a less complex, "reduced-order," or "surrogate" model. In this study, the polynomial chaos (PC) surrogate construction is applied and briefly introduced below (Le Maître & Knio, 2010). The surrogate model (M^{PC}) is built by expressing the mechanistic model output as a truncated polynomial expansion of uncertain model parameters which approximates all the associated QoIs, indexed by i, as:

$$M_i(\boldsymbol{\kappa}) \approx M_i^{PC}(\boldsymbol{\kappa}) = \sum_{l=0}^{P} c_{il} \Psi_l(\boldsymbol{\kappa}), \tag{18}$$

where c_{il} are polynomial coefficients, $\Psi_l(\boldsymbol{\kappa})$ are multivariate orthogonal polynomials, and $P + 1 = \frac{(m+q)!}{m!q!}$ is the number of terms in the PC expansion, where m is the number of stochastic dimensions (equals to the number of uncertain parameters), and q is the highest polynomial order of the expansion Equation 18 that includes all polynomial bases up to a total order q. The coefficients c_{il} are estimated from the multiple runs of the model M using random samples of the parameter set $\boldsymbol{\kappa}$. The model outputs of QoI are used to compute the coefficients c_{il} by using Gaussian quadrature projection (Smolyak, 1963), regression (Berveiller et al., 2006; Blatman & Sudret, 2008, 2011), or Bayesian approaches such as Bayesian Compressive Sensing method (Babacan et al., 2009; Sargsyan et al., 2014). The latter is applied in this work as it allows an adaptive selection of polynomial bases that are relevant for the surrogate. The efficacy of the surrogate modeling used for all types of data in Sec. 3 is validated in Supporting Information S1 (Text S6). In the following, we will explicitly highlight the spatio-temporal conditions ($\boldsymbol{x}$, t) that these outputs are computed at and denote the data and the model $\boldsymbol{Y}(\boldsymbol{x}, t)$ and $M(\boldsymbol{\kappa}, \boldsymbol{x}, t)$, respectively. Note that the surrogate construction described in this section assumes individual PC approximations for each QoI, indexed as $i = 1, 2, \ldots, Q$. A major challenge in this formulation is that Q may be too large for spatio-temporal fields associated with conditions ($\boldsymbol{x}$, t), making the construction of Q surrogates computationally expensive. For that reason, we will initially reduce the dimensionality of the model outputs using Karhunen-Loève expansion, described next.

2.3.3. Karhunen-Loève Expansion

A given QoI output of a mechanistic model $M(\boldsymbol{\kappa}, \boldsymbol{x}, t)$ can be considered to represent a stochastic process, given the uncertainty associated with the parameter vector $\boldsymbol{\kappa}$. The size Q of the QoI output from the model M depends on the characteristics of the conditions of interest (i.e., the physical dimensions of space and time duration of simulation) and is often large, consisting of (10^3–10^5) spatial and temporal values. The efficiency of traditional simulation-based inference methods such as approximate Bayesian computation with or without tractable likelihood highly relies on the dimension of data (Cranmer et al., 2020). According to the Karhunen-Loève (KL) expansion (Karhunen, 1947; Le Maître & Knio, 2010; Loève, 1948), a stochastic process (in this case, a QoI output of $M(\boldsymbol{\kappa}, \boldsymbol{x}, t)$) can be represented by a sequence of zero-mean, unit-variance, uncorrelated variables ξ_j as:

$$M(\boldsymbol{\kappa}, \boldsymbol{x}, t) = \overline{M}(\boldsymbol{x}, t) + \sum_{j=1}^{\infty} \xi_j(\boldsymbol{\kappa}) \sqrt{\mu_j} \varphi_j(\boldsymbol{x}, t), \tag{19}$$

where $\overline{M}(\boldsymbol{x}, t)$ is the mean of model outputs, μ_j and $\varphi_j(\boldsymbol{x}, t)$ are the eigenvalues and eigenfunctions of the unscaled covariance matrix $cov[M(\boldsymbol{\kappa}, \boldsymbol{x_i}, t_i), M(\boldsymbol{\kappa}, \boldsymbol{x_j}, t_j)]$, respectively (the pairs $(\boldsymbol{x_i}, t_i)$ and $(\boldsymbol{x_j}, t_j)$ are points in the space and time domain), and $\xi_j(\boldsymbol{\kappa})$ are uncorrelated random variables called KL coefficients derived by solving the linear system. In practice, the first J eigenvalues and their corresponding eigenfunctions are selected. That is, we select the smallest J such that $\sum_{j=1}^{J} \mu_j / \sum_{j=1}^{\infty} \mu_j > 0.95$, that is, at least 95% of variance contained in $M(\boldsymbol{\kappa}, \boldsymbol{x}, t)$ output of QoI is captured. If the spatio-temporal model outputs exhibit strong correlations, a relatively small number J as the upper summation limit in Equation 19 can make the estimation of the right-hand-side part of Equation 19 sufficiently close to $M(\boldsymbol{\kappa}, \boldsymbol{x}, t)$ as we have previously observed in Ivanov et al. (2021). Furthermore, if the mechanistic model is believed to accurately simulate the behavior of a real system and therefore can perform well with respect to the observations of QoIs, the eigenvalues and eigenfunctions inferred from Equation 19 can be viewed as representative of the process governing the variation of QoIs as well. The impact of model discrepancy is discussed in Supporting Information S1 (see Text S2). Therefore, observational data $\boldsymbol{Y}(\boldsymbol{x}, t)$ on QoIs can be also projected to the same eigenspace defined by μ_j and $\varphi_j(\boldsymbol{x}, t)$ of Equation 19 as

$$\boldsymbol{Y}(\boldsymbol{x}, t) = \overline{M}(\boldsymbol{x}, t) + \sum_{j=1}^{\infty} \eta_j \sqrt{\mu_j} \varphi_j(\boldsymbol{x}, t), \tag{20}$$

where η_j, the KL coefficients for $\boldsymbol{Y}(\boldsymbol{x}, t)$, are computed via projection similar to how KL coefficients $\xi_j(\boldsymbol{\kappa})$ of the model are computed. The observations $\boldsymbol{Y}(\boldsymbol{x}, t)$ can be approximately estimated by setting J as the upper summation limit in Equation 20, that is, using only the largest J eigenvalues and their corresponding eigenfunctions and KL coefficients η_j. The data truncation will induce additional noise in the likelihood approximation in theory. However, it is an acceptable price for having a tractable and fast-to-evaluate likelihood. In practice, increasing J induces more accurate likelihood approximation, but the overall cost of performing MCMC becomes unfeasibly large defeating the purpose of the KL-based likelihood. The mechanistic model parameters can then be inferred following the Bayesian inference approach taking the J eigen-variables as effective QoIs, that is, by using J coefficients $\eta = (\eta_1, \ldots, \eta_j)$ as "observations" $\boldsymbol{Y}$ that need to be reproduced by the model $M(\boldsymbol{\kappa})$, given the uncertain coefficients $\xi_j(\boldsymbol{\kappa})$ ($j = 1, 2, \ldots, J$) depending on the vector of uncertain model parameters $\boldsymbol{\kappa}$ (i.e., as in Sec. 2.3.1). In other words, the likelihood function described in Equation 16 is now approximated by:

$$L(\boldsymbol{Y}|\boldsymbol{\kappa}) \approx L(\boldsymbol{\eta}|\boldsymbol{\kappa}) = \prod_{j=1}^{J} \frac{1}{\sqrt{2\pi\sigma_j^2}} \exp\left(-\frac{\left(\eta_j - \xi_j(\boldsymbol{\kappa})\right)^2}{2\sigma_j^2}\right). \tag{21}$$

Besides the overall computational savings, this independent and identically distributed Gaussian likelihood is a reasonable assumption in the KL-reduced space, as opposed to the full space, as the KL coefficients ξ_j's are uncorrelated, zero mean and unit variance by construction. The data standard deviation σ_j corresponds to each eigenvalue μ_j and is weighted by the normalized square root of the reciprocal of μ_j, that is,

$$\sigma_j^2 = \frac{J}{\mu_j} \Big/ \left(\sum_{j=1}^{J} \frac{1}{\mu_j} \right), \tag{22}$$

An advantage of this treatment is that if the original QoI dimension Q is very large (e.g., $\mathcal{O}(10^3$–$10^5)$), a considerably smaller number J (e.g., $\mathcal{O}(10^0$–$10^1)$) of effective QoIs is obtained using this approach. Consequently, J surrogate models are needed, which substantially improves computational performance of the UQ machinery (Ivanov et al., 2021).

As a result, a PC surrogate model can be built for $\xi_j(\boldsymbol{\kappa})$ as:

$$\xi_j(\boldsymbol{\kappa}) \approx \xi_j^{PC}(\boldsymbol{\kappa}) = \sum_{l=0}^{P} c_{jl} \Psi_l(\boldsymbol{\kappa}), \tag{23}$$

Combining Equation 23 and Equation 19 leads to a joint KL-PC expansion for the mechanistic model:

$$M(\boldsymbol{\kappa}, \boldsymbol{x}, t) \approx \overline{M}(\boldsymbol{x}, t) + \sum_{j=1}^{J} \sum_{l=0}^{P} c_{jl} \Psi_l(\boldsymbol{\kappa}) \sqrt{\mu_j} \varphi_j(\boldsymbol{x}, t). \tag{24}$$

2.3.4. Overall UQ Workflow

The general procedure of parameter inference using UQ is described below.

1. The prior distributions for each parameter (i.e., the elements of $\boldsymbol{\kappa}$) are determined from a priori knowledge (e.g., uniform or Gaussian priors with range or mean and variance found from literature, respectively).
2. Parameter values of $\boldsymbol{\kappa}$ are randomly generated from their priors N times, forming a set of N parameter vectors $\boldsymbol{\kappa}^{(n)}$, $n = 1, 2, \ldots, N$.
3. N forward simulations of QoIs are conducted using the model $M(\boldsymbol{\kappa}, \boldsymbol{x}, t)$ with $\boldsymbol{\kappa}^{(n)}$; such QoI outputs are called the *training set*.
4. The space-time dimensions of the QoIs from $M(\boldsymbol{\kappa}, \boldsymbol{x}, t)$ and the data $\boldsymbol{Y}(\boldsymbol{x}, t)$ are reduced using the KL expansions in Equations 19 and 20 resulting in the independent variables $\xi_j(\boldsymbol{\kappa})$, and η_j respectively.
5. A PC surrogate model $\xi_j^{PC}(\boldsymbol{\kappa})$ is built to mimic each j-th $\xi_j(\boldsymbol{\kappa})$ as in Equation 23, leading to a joint KL-PC expansion in Equation 24.
6. In Equations 13–17, the QoI observational data array $\boldsymbol{Y}$ is replaced by the set of J values of η_j and the model output on QoIs $M(\boldsymbol{\kappa},\boldsymbol{x},t)$ is replaced by the joint KL-PC expansion, and Bayesian inference is performed with the likelihood approximated as in Equation 21.
7. The joint posterior distribution for $\boldsymbol{\kappa}$ in Equation 17 is sampled via MCMC, including the estimate for the maximum a posteriori (MAP) parameter vector $\boldsymbol{\kappa}^{MAP}$.
8. The final visual and statistical diagnostics are made by comparing the estimation of the QoI using the joint KL-PC expansion in Equation 24 with $\boldsymbol{\kappa}^{MAP}$ and the observation data with posterior predictive bounds representing the uncertainty in model predictions (see Text S5 in Supporting Information S1 for posterior predictive construction details).

2.4. Surface Ground Heat Flux Reconstruction

2.4.1. G_0 Data Are Available During Snow-Free Season

Data on G_0 can sometimes be obtained from field measurements but such data are mostly reliable during snowpack-free seasons because the flux magnitudes are mostly larger than zero. During snow season, measurements are often noisy due to the phase change of water in the vicinity of the heat flux plate and advective heat flux related to infiltration caused by snowmelt. Flux G_0 can also be inferred from typical global scale model outputs based on the surface energy balance (Section 1). However, as estimates of the change of the snowpack internal energy are never provided, this approach cannot be applied to derive G_0 during snowpack seasons. In this case, the available G_0 data during snowpack-free season can be used as a reference to infer the parameters representing soil thermal properties in the HOD model. Once the parameters are estimated, the continuous heat

flux G_0 can be reconstructed using near-surface temperature time series (more accurately measured and more readily available) following the procedure described below.

The prior distributions of the HOD model parameter set $\boldsymbol{\kappa}^{HOD} = (c_h, k_{dry}, k_s)$ obtained using the parameter separation method (Section 2.1.2) are first derived from available information on soil properties such as SoilGrids, a digital soil mapping product based on a global compilation of soil profile data (Hengl et al., 2017). Details on the derivation of the parameter prior distributions are provided in Supporting Information S1 (Text S1). After N arrays of $\boldsymbol{\kappa}^{HOD}$ are generated according to their prior distributions, a set of N series of ground heat flux (G_1^{HOD}) at a shallow depth z_1 (not exceeding few cm and it was 5∼10 cm in this study) are simulated using the time-series of near-surface soil temperature and moisture (if available) at the same depth z_1 using Equation 1. In order to get a close approximation of the surface ground heat flux, the heat storage and water phase change transformations in the top soil layer between z_0 and z_1 should be accounted for. Because depth z_1 is deliberately chosen to be very shallow, the approximate *surface* ground heat flux $\tilde{G}_0$ is proportional to G_1^{HOD} with a scaling factor α to account for the effect of heat storage between the surface and z_1, that is, $\tilde{G}_0 = \alpha G_1^{HOD}$. To estimate the N series of $\tilde{G}_0$ from G_1^{HOD}, N values of α are sampled from a uniform prior distribution. Available series of the surface ground heat flux (from observations, GCM model, or reanalysis product estimates) for all snowpack-free seasons are then concatenated into a single series. They are used as available data on target QoIs (denoted as G_0^{TGT}) and the similarly concatenated simulations of $\tilde{G}_0$ are used as the training set in the UQ machinery (see Section 2.3) to infer a joint posterior distribution of the parameter set $\boldsymbol{\kappa} = (\boldsymbol{\kappa}^{HOD}, \alpha)$. The MAP estimates $\boldsymbol{\kappa}^{MAP} = (\boldsymbol{\kappa}^{HOD,MAP}, \alpha^{MAP})$ and the corresponding marginal posterior distributions are estimated from the joint distribution. Finally, the surface ground heat flux for both snowpack and snowpack-free seasons can be reconstructed by the HOD model using soil temperature and moisture (if available) data series at z_1 and the inferred MAP parameter estimates: $\tilde{G}_0^{MAP} = \alpha^{MAP} G_1^{MAP}$, where $G_1^{MAP} = G_1^{HOD}\left(\boldsymbol{\kappa}^{HOD,MAP}\right)$. The uncertainty of the reconstructed $\tilde{G}_0$ is represented by the posterior predictive bounds computed from the surrogate model with parameter sets sampled from the joint posterior distributions (see Text S5 in Supporting Information S1).

2.4.2. G_0 Data Are Unavailable

When data or estimates on ground heat flux G_0 are unavailable, it is infeasible to generate a target (G_0^{TGT}) in the parameter inference process for the HOD model as in Sec. 2.4.1. In this case, the HOD model is combined with the physically-based freeze-thaw numerical model described in Section 2.2 (Sheshukov & Egorov, 2002) to simulate soil temperatures. These temperatures T_i measured at depth z_i (i = 1, 2, …, n) are used as the target QoI (i.e., $T^{TGT} = T_i$). Identical to the process described in Sec. 2.4.1, the prior distributions for the parameter set $\boldsymbol{\kappa}$ are constructed first, but here both the parameters used in the freeze-thaw numerical model, the HOD model, and the scaling factor α are included in the parameter set $\boldsymbol{\kappa}$, that is, $\boldsymbol{\kappa} = (\boldsymbol{\kappa}^{NUM}, \boldsymbol{\kappa}^{HOD}, \alpha)$. After that, N arrays of $\boldsymbol{\kappa}$ are generated from their priors. For each parameter set of $\boldsymbol{\kappa}$, first, the heat flux G_1^{HOD} at the shallowest depth z_1 is computed from the measured soil temperature T_1 by the HOD model using $\boldsymbol{\kappa}^{HOD}$. Then the approximate surface ground heat flux is calculated as $\tilde{G}_0 = \alpha G_1^{HOD}$. Next, soil temperatures at the same depths of the observation, T_i^{NUM} (i = 1, 2, …, n), are simulated by the freeze-thaw numerical model using $\boldsymbol{\kappa}^{NUM}$ and with $\tilde{G}_0$ set as the top boundary condition. The N sets of simulated soil temperatures T_i^{NUM} form the training set. Finally, the joint posterior distribution of $\boldsymbol{\kappa}$ can be inferred by the UQ machinery (Sec. 2.3) with the training set and T^{TGT}.

After the MAP estimates $\boldsymbol{\kappa}^{MAP}$ and the corresponding marginal posterior distributions are estimated, the surface ground heat flux can be reconstructed as $\tilde{G}_0^{MAP} = \alpha^{MAP} G_1^{MAP}$, where $G_1^{MAP} = G_1^{HOD}\left(\boldsymbol{\kappa}^{HOD,MAP}\right)$. Since the measurements of G_0 are not available, the approximated flux $\tilde{G}_0^{MAP}$ cannot be directly validated. However, by applying $\tilde{G}_0^{MAP}$ as the top boundary condition in the numerical model, its accuracy level can be corroborated indirectly by the magnitude of the error between the simulated and observed soil temperatures, as well as the degree of deviation of the model parameters' values with respect to their physically realistic range.

2.4.3. Soil Moisture Data Are Unavailable

When soil moisture data are unavailable, the HOD model parameters are determined assuming saturated soil with single phase of water, that is, $\theta_{liq} = \theta_{sat}$, $\theta_{ice} = 0$ for $T > 0$°C and $\theta_{liq} = 0$, $\theta_{ice} = \theta_{sat}$ for $T < 0$°C. For this

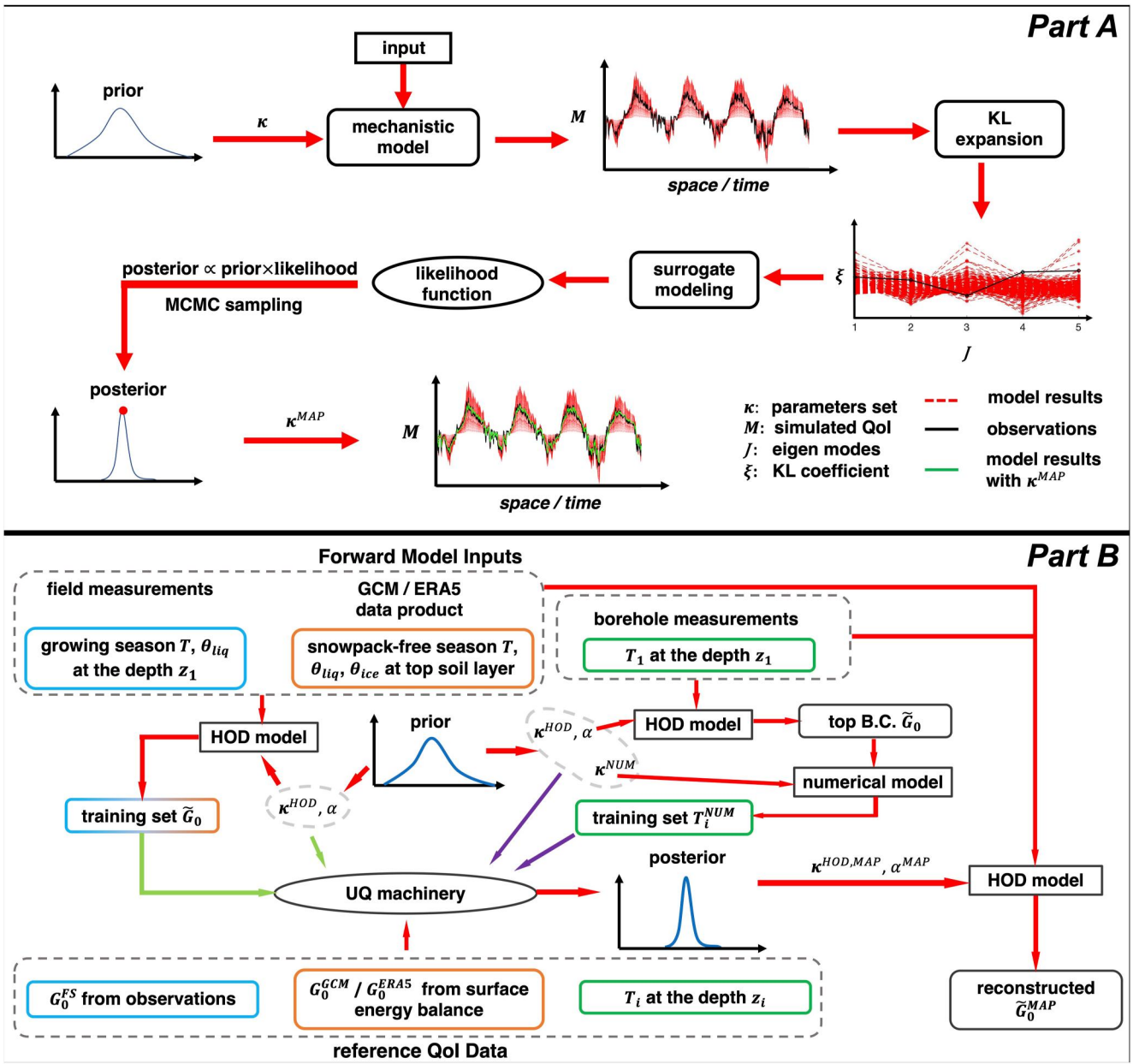

Figure 1. Part (a): visualization of the overall UQ workflow described in Section 2.3.4. Part (b): an overview of the surface ground heat flux G_0 reconstruction workflow for the four types of data presented in Section 3.

case, the parameter k_{dry} is no longer required in the computation, and the parameters to be inferred in the set are $\boldsymbol{\kappa} = (c_h, k_s, \theta_{sat})$.

3. Data

Four types of data are used in this study to test the performance of the developed process of heat flux G_0 reconstruction: (a) in situ field measurements of soil temperature, moisture, and snowpack-free season G_0 at a shallow depth; (b) GCM outputs and (c) ERA5-Land reanalysis products of soil temperature and moisture for the topmost soil layer, and snow-free season G_0 derived from the surface energy balance; and (d) borehole data of soil temperature measured at four depths. An illustration of the general workflow is illustrated in Figure 1.

3.1. Field Measurements

Soil temperature, moisture, and ground heat flux were monitored at several sites located in the eastern slope of the Polar Urals of Russia since 2013. Data from one plot (LPTEG-TREES-1, N66°53′55″, E66°45′27″, the location is shown in Figure S6 in Supporting Information S1) are used to apply the developed process in Sec. 2.4.1. This site is vegetated with Siberian larch (~5 m height). The distances between individual trees are several meters. The ground surface is covered by an organic or peat layer (~5 cm thick), with clayish soil underlain. Specifically, ground heat flux was measured using soil heat flux plates (HukseflUXUSA Inc. HFP01 Heat Flux Sensor). The plate was placed horizontally in the soil and in tight contact with soil medium. In most Arctic regions, a peat layer composed mainly of soil organic matter is present above mineral soil due to its slow rate of decomposition (El Sharif et al., 2019). The porous peat layer of heterogeneous thickness and thermal properties makes it difficult to measure conductive heat flux due to poor sensor-medium contact. Hence, the heat flux plate was installed at 6 cm below the mineral soil surface covered with a peat layer of ~6 cm thickness. At the same location where the heat flux plate was buried, three temperature sensors (Campbell Scientific Inc. 109 and 107 thermistors, analog) were installed. Two thermistors were placed at 2 and 4 cm depth in the mineral soil to measure temperature gradient and one thermistor was placed at 2 cm below the peat layer surface for peat layer temperature monitoring. The mineral soil temperature and moisture are measured using a Time-Domain Reflectometer (TDR) sensor (Campbell Scientific Inc. CS655, digital) with two prongs inserted at 1.5 and 4.5 cm below the mineral soil surface. The rate of change of soil thermal energy storage E_s above the heat flux plate, $\frac{dE_s}{dt}$ (W m^{-2}), is computed from the measured temperature and moisture of both peat and mineral soil: $\frac{dE_s}{dt} \approx \frac{\Delta E_s}{\Delta t} = \frac{\Delta T\, c_v\, \Delta z_s}{\Delta t}$, where ΔT is the hourly soil temperature change, Δz_s is the thickness of the mineral soil over the heat flux plate, and c_v is calculated by Equation 8 with c_h estimated by Equation S1.1a in Supporting Information S1. Ground heat flux at the surface for this plot (G_0^{FS}) is reconstructed as the measured flux corrected by $\frac{dE_s}{dt}$ (Campbell Scientific, 2016).

One issue with the field measurements is that liquid soil water content is available only when the soil temperature is above 0°C. This is due to the physical design of the TDR based on the time domain principle (Jones et al., 2002). Volumetric water content is derived based on the dielectric permittivity of the medium, so the sensor can only detect the signal of liquid water with high permittivity (Campbell Scientific, 2018). Due to this complication, ground heat flux is reconstructed using hourly temperature T at 2 cm in the peat layer and θ_{liq} at 2 cm in the mineral soil layer, and G_0^{FS} during the growing season of 2019 when near surface ice content $\theta_{ice} = 0$.

In the context of the method described in Section 2.4.1, the measured time series of G_0^{FS} is the target QoI (denoted as G_0^{TGT} earlier). The ensemble of $\tilde{G}_0$ is computed using $N = 500$ parameter sets to produce the training set. The number of eigenvalues and eigenfunctions identified in the KL expansion is $J = 2$, which is drastically smaller than the size of the input data ($Q = 1{,}700$ data points). The truncation order used for each polynomial surrogate model is $q = 4$. More details on the KL expansion estimates are presented in Supporting Information S1 (Text S2).

3.2. GCM Data Product

Global climate models are developed based on physical processes for simulating past, current, and future climate trajectories. Main components of the land surface energy budget including R_n, H, and λE are provided explicitly in GCM outputs, but not G_0. Theoretically, the latter can be derived from the energy balance equation, that is,

$$G_0 = R_n - H - \lambda E. \tag{25}$$

During snow-free summer period, the heat flux derived using GCM outputs of surface energy budget components (as discussed in Introduction) can be considered as GCM-modeled heat flux at the ground surface (G_0^{GCM}). Conversely, the components of the snow surface energy budget are never explicitly provided in GCM outputs for snowpack period, and therefore G_0 cannot be derived from Equation 25 during snowpack conditions. Nonetheless, when available, GCM simulated temperature of the topmost soil layer along with the derived summer heat flux G_0^{GCM} can be jointly used to reconstruct G_0 following the process described in Sec. 2.4.1 and illustrated in Figure 1.

In this study, GCM models from the Coupled Model Intercomparison Project Phase 6 (CMIP6) (Eyring et al., 2016) were selected to illustrate the method based on the following criteria. First, a GCM model must

provide near-surface soil temperature and water content in order to enable applying the parameter separation approach (see Sec. 2.1.2). Second, the model should provide outputs of all components of the surface energy budget (i.e., R_n, H, and λE) to derive snowpack-free season G_0^{GCM}, to infer soil thermal properties using the UQ machinery. Third, the model should also provide snow coverage conditions, such as snow depth, to separate the snowpack period from the rest of the year. After identifying the models, the required daily outputs (i.e., T, θ_{liq}, θ_{ice} in the top soil layer, R_n, H, and λE) for the historical period from 1981 to 2014 were downloaded.

The methodology is tested here using daily historical outputs from one exemplary member of the CMIP6 models: CESM2 (Danabasoglu et al., 2020). The results are presented for the grid cell covering the location of a borehole site used in this study ("Marre-Sale," see Sec. 3.4). Soil temperature and moisture of the 2-cm topsoil layer of the CESM2 are used to compute the training set $\tilde{G}_0$. Summer period heat flux computed as the residual term of the surface energy budget (G_0^{GCM}) from Equation 25 is concatenated and used as G_0^{TGT} in the UQ machinery. For this case, the training set size is $N = 500$, and the number of eigenvalues and eigenfunctions identified is $J = 2$, which is much smaller than the input size Q of 3,889 data points (i.e., the number of snowpack-free days during 1981–2014) in the CESM2 output time series. The truncation order of the surrogate polynomial expansion is $q = 4$.

3.3. ERA5-Land Reanalysis Product

Reanalysis products can theoretically provide the most complete description of past climate by assimilating observations and dynamic model forecasts (Decker et al., 2012; Lindsay et al., 2014). One of the state-of-the-science products is the fifth generation ECMWF atmospheric reanalysis (ERA5) of the global climate (Hersbach et al., 2020). The new land component of ERA5 (ERA5-Land) provides outputs with higher spatial resolution ($0.1° \times 0.1°$) suitable for land application (Muñoz-Sabater et al., 2021). As in Sec. 3.2, data for variables required to reconstruct G_0: T, θ in the top soil layer, R_n (derived by shortwave and longwave radiation), H, and λE from 1981 to 2020 were downloaded.

The ground heat flux reconstruction process described in Sec. 2.4.1 is applied with outputs from ERA5-Land product at the daily scale. The grid cell that covers the same borehole site in Marre-Sale is considered. The training set $\tilde{G}_0$ is computed by the HOD model using soil temperature and moisture in the first soil layer (7 cm thick). The target QoI G_0^{TGT} is the concatenated snowpack-pack free season G_0^{ERA5} derived from energy balance Equation 25. The training set size is $N = 500$, truncation order $q = 4$, and the number of eigenvalues and eigenfunctions identified is $J = 1$ (i.e., again, drastically smaller than the input size Q of 3,511 data points in the downloaded ERA5-Land time series).

3.4. Borehole Measurements

Since the most recent International Polar Year (2007–2009), a global data set of permafrost temperature has been developed based on borehole measurements. Borehole soil temperature measurements starting at shallow depths (~10 cm) are available from the Circumpolar Active Layer Monitoring (CALM) program (Brown et al., 2000). Borehole measurements indicate one of the fastest-warming rates of ground temperature is in Northwestern Siberia (Biskaborn et al., 2019). Measurements from the Marre-Sale borehole site (N69°43', E66°51', the location is shown in Figure S6 in Supporting Information S1) (Malkova et al., 2022; Melnikov et al., 2004; Vasiliev et al., 2008) representing this region were selected to reconstruct G_0 using the proposed approach. The surface is covered with dwarf shrub, moss, and lichen combining with sedge-moss and mud. The soil underlain is sandy and clayey. In general, an "ideal" set of characteristics for borehole locations includes (a) near-surface (few cm) temperature measurements, (b) long-term continuous records, and (c) measurements for several depths. Daily soil temperatures are available at 5 cm, 50 cm, 1 m, 2 m depth for this borehole. Time series segments during 1 December 2006 to 31 December 2010 with the most complete and continuous temperature measurements are used henceforth. Missing data points (12 in total, i.e., the gap is 12 days) of the observed T_1 series are filled by linear interpolation, resulting in the total of $Q = 1{,}492$ data points. Flux $\tilde{G}_0$ is then computed with the HOD model using the gap-filled T_1 and used as the boundary input for the numerical model. Since soil moisture was not measured in the borehole, assumptions in Sec. 2.4.3 are used. Soil temperature measured at the four depths are concatenated head to tail, shallow to deep, to build a one-dimensional array. This array is used as T^{TGT} in the UQ machinery (see Text S4 in Supporting Information S1 for parameter inference of the numerical model in detail). The training set is formed by $N = 500$ arrays of simulated soil temperatures (concatenated in the same manner as described above for each simulation run). In the parameter inference process, we set the polynomial order $q = 4$, and the KL expansion

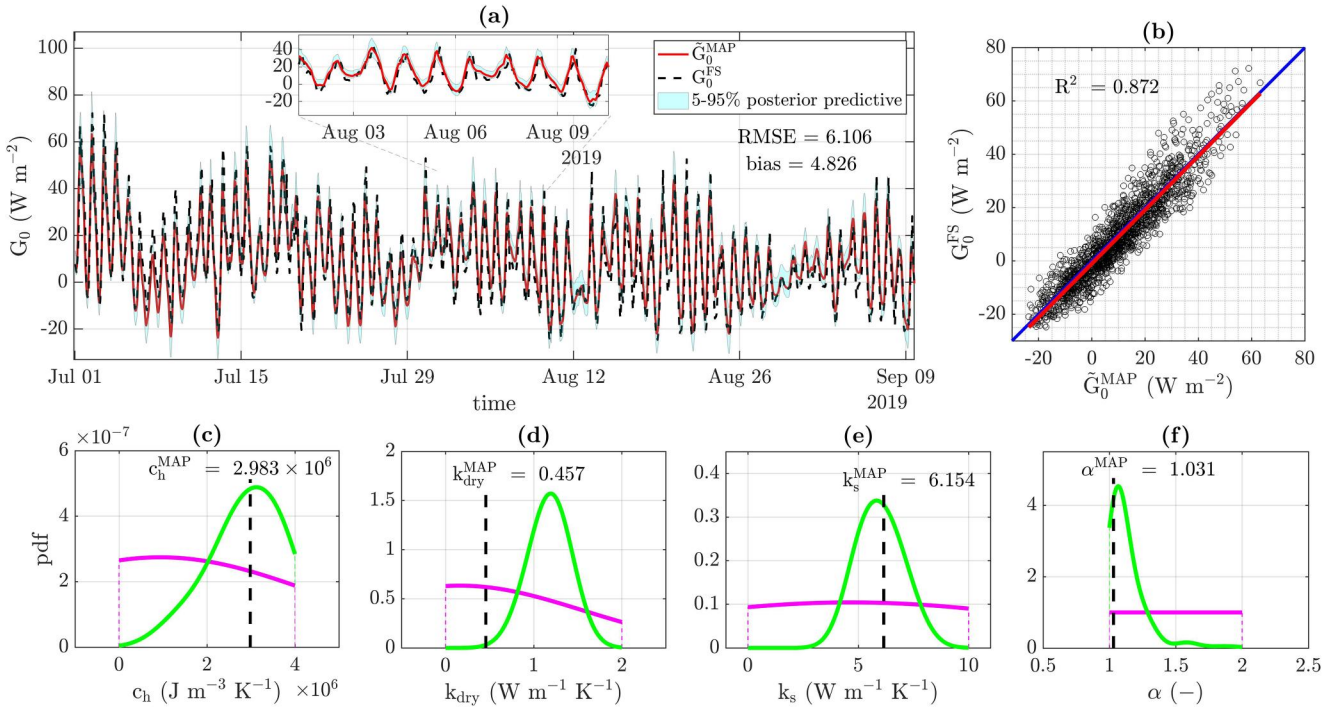

Figure 2. (a) Observed G_0^{FS} (black dashed line) and reconstructed $\tilde{G}_0^{MAP}$ (red solid line) heat flux series at the hourly resolution with 5%–95% posterior predictive bounds (cyan area). The reconstruction is based on the process described in Section 2.4.1 using field-measured soil temperature and moisture (Section 3.1). (b) The scatter plot and linear regression (red solid line) fitted for $\tilde{G}_0^{MAP}$ and G_0^{FS} (the blue solid line is 1:1) with slope = 1.009 and intercept = −0.999. "R^2" is the coefficient of determination of the regression. (c)–(f) Kernel density estimation (KDE) of the marginal posterior distributions for c_h, k_{dry}, k_s, and α (green curves) derived as described in Section 3.1. Values of MAP parameter estimates (i.e., c_h^{MAP}, k_{dry}^{MAP}, k_s^{MAP}, and α^{MAP}) are indicated by the vertical black dashed lines in (c)–(f). Parameter prior distributions are shown as the magenta curves.

retains $J = 6$ eigen-modes. The numerical model simulation setups are described in Supporting Information S1 (Text S3).

4. Results

4.1. Field Measurements

The reconstructed G_0^{FS} from heat flux plate measurements (black dashed line) and the reconstructed $\tilde{G}_0^{MAP}$ from temperature and moisture measurements (red solid line) at the field site are shown in Figure 2a. The variance of $\tilde{G}_0$ is presented by 5%–95% posterior predictive bounds (cyan area, see Text S5 in Supporting Information S1 for details). The accuracy of the reconstructed $\tilde{G}_0^{MAP}$ is assessed using the root mean square error $\text{RMSE} = \sqrt{\frac{\sum_{i=1}^{Q}\left(\tilde{G}_0^{MAP}(i) - G_0^{FS}(i)\right)^2}{Q}} = 6.106$ and $\text{bias} = \frac{\sum_{i=1}^{Q}\left|\tilde{G}_0^{MAP}(i) - G_0^{FS}(i)\right|}{Q} = 4.826$ (W m^{-2}), as well as by the coefficient of determination (R^2) of linear regression in Figure 2b. Figures 2c–2f shows the fitted marginal posterior distributions for c_h, k_{dry}, k_s, and α (green curves) and the corresponding MAP estimates along with their corresponding prior distribution (magenta curves, see Text S1 in Supporting Information S1 for details). The inferred MAP values are within the same order of magnitude of typical ranges of soil properties: $c_h \sim 0.2$ to 1.4×10^6 (J m^{-3} K^{-1}), $k_{dry} \sim 0.05$ to 0.3 (W m^{-1} K^{-1}), and $k_s \sim 0.25$ to 9.0 (W m^{-1} K^{-1}) (Lawrence & Slater, 2007).

4.2. GCM Data Product

The concatenated series of snowpack-free seasons for reconstructed $\tilde{G}_0^{MAP}$ and G_0^{GCM} from CESM2 outputs were computed from 1981 to 2014 and Figure 3a shows a time interval between 2010 and 2014 to illustrate a higher

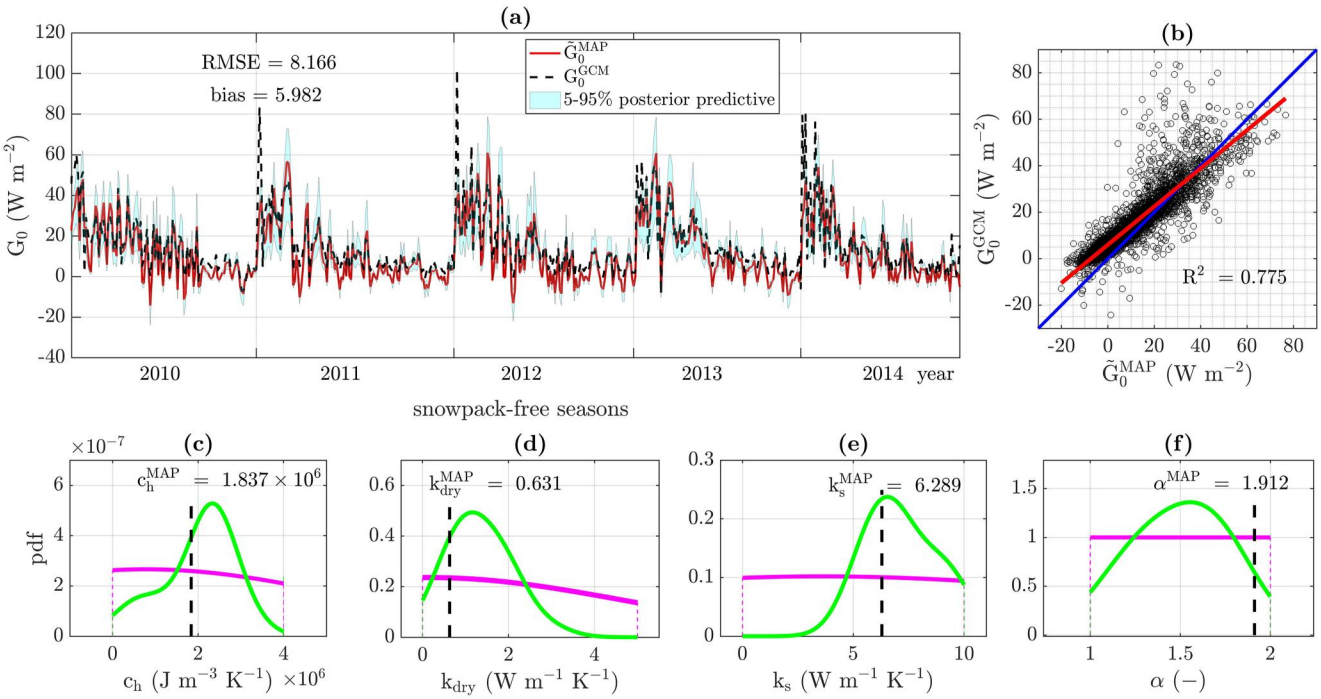

Figure 3. (a) Concatenated $\tilde{G}_0^{MAP}$ (red solid line) and G_0^{GCM} (black dashed line) series for snowpack-free seasons at the daily resolution with 5%–95% posterior predictive bounds (cyan area). $\tilde{G}_0^{MAP}$ is reconstructed following the process in Section 2.4.1 using temperature and moisture of the topmost soil layer in CESM2 (Section 3.2). (b) The scatter plot and linear regression (red solid line) fitted for $\tilde{G}_0^{MAP}$ and G_0^{GCM} (the blue solid line is 1:1) with slope = 0.822 and intercept = 6.002. (c)–(f) KDE of the marginal posterior distributions for c_h, k_{dry}, k_s, and α (green curves) derived as described in Section 3.2. Vertical black dashed lines indicate values of MAP parameter estimates (i.e., c_h^{MAP}; k_{dry}^{MAP}; k_s^{MAP}, and α^{MAP}). Parameter prior distributions are shown as the magenta curves.

level of detail. Posterior predictive bounds display the variance of $\tilde{G}_0$. The scatter plot between $\tilde{G}_0^{MAP}$ and G_0^{GCM} in Figure 3b shows a lower coefficient of determination (R^2) than that in Figure 2b. RMSE and bias are 8.166 and 5.982 (W m^{-2}), respectively. The marginal posterior distributions inferred for c_h, k_{dry}, k_s, and α and their corresponding MAP values are presented in Figures 3c–3f. As with the field observations, the MAP values of c_h, k_{dry}, and k_s are consistent with typical values for these soil properties (see Sec. 3.1 for the ranges of these properties).

4.3. ERA5-Land

Figure 4a compares the concatenated $\tilde{G}_0^{MAP}$ and G_0^{ERA5} for snowpack-free seasons in the time interval from 2011 to 2015, with RMSE = 5.774 and bias = 4.619 (W m^{-2}). Variance of $\tilde{G}_0$ is presented by the posterior predictive bounds. Figure 4b presents the corresponding scatter plot with linear regression. The R^2 value is similar to that estimated for the GCM data product. The MAP values of c_h, k_{dry}, and k_s are similarly within the typical ranges for soil properties as shown in Figures 4c–4f.

4.4. Borehole

Figures 5a–5d compare the simulated temperatures from the numerical model that use $\tilde{G}_0^{MAP}$ as the top boundary input and the borehole measurements at different depths down to 2 m with the posterior predictive bounds representing the uncertainty of simulation results. Figures 5e–5h present the corresponding comparisons as a scatter plot format. As the figure shows, the posterior predictive bounds predominantly contain the timeseries of observations. The inferred MAP estimates of the model parameters and their corresponding marginal posterior distributions are presented in Supporting Information S1 (see Figure S4) demonstrating that they are in a physically realistic range.

10.1029/2023EA003435

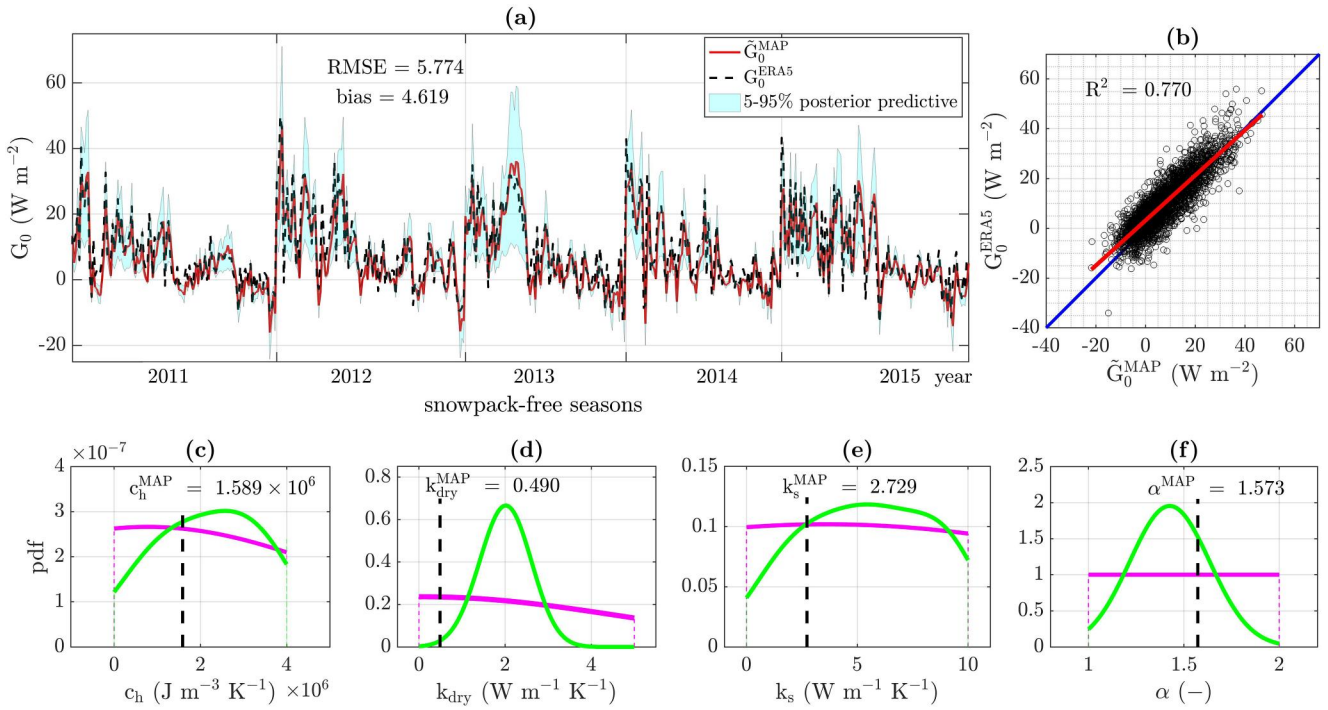

Figure 4. The same content as in Figure 3 for ERA5-Land outputs (Section 3.3). For the linear regression in (b), slope = 0.906 and intercept = 3.154.

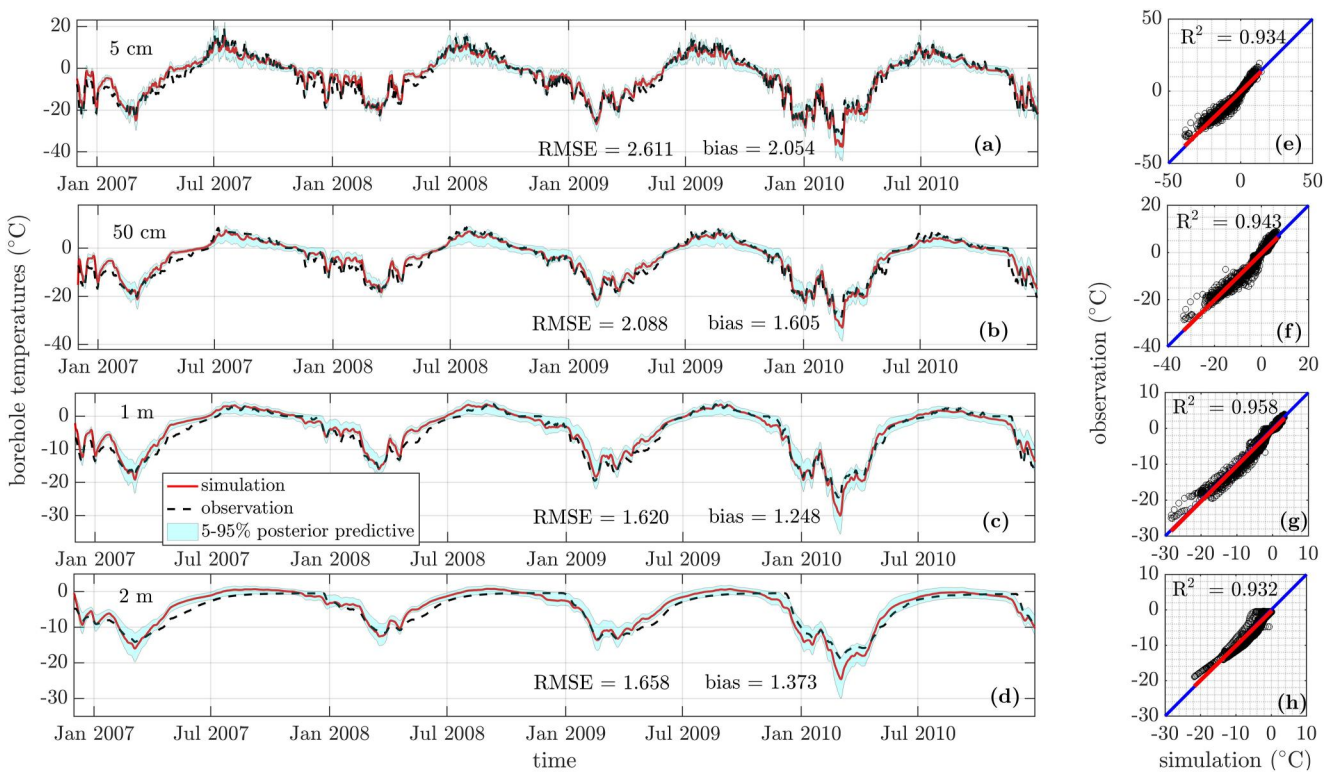

Figure 5. (a)–(d) A comparison of the temperature time series based on simulations results from the numerical model described in Section 2.2 using $\tilde{G}_0^{MAP}$ and the daily temperature measurements at different depths at Marre-Sale from December 2006 to December 2010 with 5%–95% posterior predictive bounds (cyan area). (e)–(h) The corresponding scatter plots and linear regression (red solid line) between simulated and observed temperature.

5. Discussion

5.1. UQ Efficiency

The demonstrated results confirm the credibility and skill of the ground heat flux reconstruction framework in various settings. As compared to previous efforts of parameter tuning, one of the advantages of using the UQ machinery in the developed approach is the significant improvement of computational efficiency due to the drastically decreased dimensionality of QoIs using the KL expansion and a reduced model complexity attained by PC surrogates. For all the cases presented above, the dimension of the QoI set required in the parameter inference process is reduced from $\mathcal{O}(10^3)$ to $\mathcal{O}(10^0)$. Such an extreme reduction is partially due to the high spatiotemporal correlation of the data. For example, soil temperatures for consecutive days are correlated through legacy effects (previous conditions will have impact on later conditions), and temperatures at different depths are correlated because of the diffusive heat transfer process. Even-though the KL-PC estimation assumes approximations affecting the solution accuracy during dimensionality reduction, the observational data are well captured by the KL-PC expansion and fall within the posterior predictive bounds for all types of data used. This reaffirms the consistency and generality of the developed process.

5.2. Relationship Between Joint and Marginal Posterior

Importantly, the developed methodology permits *probabilistic* assessment of surface ground heat flux and model parameters used in the heat flux reconstruction. The MAP estimates of individual parameters (Figures 2c–2f, 3c–3f, and 4c–4f, and Figure S4 in Supporting Information S1) do not necessarily coincide with the modes of their marginal posterior distributions. This mismatch means that the joint posterior distributions incorporate strong interdependency for individual parameters. Indeed, if all marginal posterior distributions were entirely independent (and since the joint distribution in this case is simply the product of marginal distributions), then MAP estimates of individual parameters derived from the joint posterior distribution would correspond to the maxima of the corresponding marginal distributions. Another possible reason of this mismatch is the relative importance of different parameters. If the model is more sensitive to certain parameters, their posteriors will be sharper and other less important parameter posteriors will be flatter with the joint MAP estimate deviating from the marginal modes.

5.3. HOD Limitation

One limitation of the HOD model is that the analytical solution of G_0 does not take the latent heat of phase change of water into account. Nonetheless, the latent heat of the phase change within the considered shallow layer of ~5 cm is negligible compared to the total accumulative seasonal heat into or out of the ground. For example, the latent heat of phase change can be approximately calculated as $(z_1 - z_0)\phi\rho_w L$, where ρ_w is the density of liquid water (kg m^{-3}) and L is the latent heat of freezing for water (J kg^{-1}). For the case of borehole in Section 3.4, the latent heat of phase change is less than 0.03% of the cumulative diffusive flux for all seasons (calculation not shown). Therefore, the reconstructed flux G_0 is not affected by neglecting the phase change energy in the top shallow soil layer.

When soil moisture data are missing, assumptions about the soil water content need to be made, as described in Section 2.4.3. One can avoid using these assumptions by applying the HOD model in its original formulation in which only two temporally invariant variables (I and D) are required, that is, the formulation does not depend on the change in soil water content. However, the thermal properties of frozen and liquid water are different and need to be considered when reconstructing G_0 at the daily resolution as well as in numerical simulations of even finer time steps. The assumptions are overall suitable for locations in the Arctic region where the active layer is nearly saturated during the winter. During relatively short summer seasons, the reconstructed G_0 may be overestimated under the assumption of full soil saturation due to the higher thermal conductivity and diffusivity of liquid water than those of the air. Measurements of soil water content of daily or finer resolution concomitant with borehole temperature measurements may help overcome this problem. The HOD solution has been shown to be a good approximation for variable diffusivity (Wang & Bras, 1998). The diffusion equation from which HOD solution in Equation 1 is derived with a space-and-time dependent diffusivity has analytical solution through a change of variable (Fitzmaurice et al., 2004). The results presented in Sec. 4.1, 4.2, and 4.3 indicate that the modified HOD model is capable of reproducing ground heat flux accurately within a reasonable range of uncertainty.

6. Conclusion

Ground heat flux is a vital energy budget component in cold regions and its quantification is important for understanding surface mass-energy relations and subsurface thermal condition. The process developed in this study provides a useful approach for reconstructing surface ground heat flux and its probability distribution from different types of shallow soil temperature data, with or without auxiliary data (i.e., soil moisture and snowpack-free season G_0 data). The reconstructed G_0 offers an alternative data source to the laborious measurements of in situ G_0 in remote regions such as the Arctic or Antarctica. Another advantage of the proposed approach is that G_0 for all seasons can be derived as long as year-round (daily, or finer temporal resolution) soil temperature data are available, which are more straightforward to obtain in terms of relevant sensor deployment and maintenance in the field. In the case of future climate projections, the likelihood and severity of future ground heating in areas underlain by the permafrost can only be inferred from GCM projections of soil temperatures; however, the validity of these projections is questionable since GCMs typically have a simplified representation of the belowground freeze-thaw dynamics, yet available outputs do not offer flux G_0 for independent validation. Furthermore, in experience of this author group, data requests to individual GCM centers to obtain G_0 series are generally futile and therefore the developed methodology offers means for independent verification of the past heating and plausibility of the projected heating of the permafrost in the future.

The credibility of the reconstructed flux G_0 is supported by a series of results presented in the application section. The UQ machinery applied in this study is useful for parameter inference and yields estimates in a plausible range of real-world soil properties. In the meantime, the developed process can significantly increase the simulation speed for data that are highly correlated in space and time. This is especially beneficial for the case when complex models based on complex physical processes are applied.

As discussed, the reconstructed flux G_0 may be overestimated during summer due to the assumption of full saturation (when soil moisture data is not available). This assumption is acceptable for the Arctic regions considered in this study due to the relatively short summer period and low evapotranspiration potential. Suitable moisture measurements can facilitate a more accurate G_0 reconstruction.

Importantly, the reconstructed G_0 and its probability density function can be used as an upper flux boundary condition in detailed numerical physical models to evaluate the probability distribution of the subsurface thermal state in specific regional and built environment settings. This is important for understanding the future dynamics of the belowground environment. For example, the developed process can be applied to reconstruct plausible future heating scenarios of the permafrost, with respect to the Shared Socioeconomic Pathways as developed by the Intergovernmental Panel on Climate Change (IPCC). Aided by detailed physical modeling and data for a region of application, such scenarios can help better resolve the probabilistic description of permafrost future impacts on land-surface hydrology, built environment, and livelihoods of the peoples of the North.

Data Availability Statement

The soil temperature, moisture, and ground heat flux data for the LPTEG-TREES-1 field site are licensed under Creative Commons Attribution 4.0 International (CC BY 4.0) and published on Zenodo https://doi.org/10.5281/zenodo.7600654 (Zhou & Ivanov, 2023). GCM outputs are licensed under CC BY 4.0 and downloaded for the CESM2 model (Danabasoglu et al., 2020) from the CMIP6 repository https://esgf-node.llnl.gov/search/cmip6 (Eyring et al., 2016). ERA5-Land data products are licensed under the Copernicus C3S/CAMS License agreement and downloaded from the Copernicus Climate Change Service (C3S) Climate Data Store (CDS) https://doi.org/10.24381/cds.e2161bac (Muñoz Sabater, 2019). Borehole measurements are licensed under Creative Commons Attribution 3.0 Unported (CC BY 3.0) and downloaded directly CALM https://www2.gwu.edu/~calm/data/north.htm (Brown et al., 2000) public repositories. The Uncertainty Quantification Toolkit (UQTk version 3.1.2) used in this study is publicly accessible at https://github.com/sandialabs/UQTk (Debusschere et al., 2004, 2016). Soil properties used to derive parameter prior distributions are downloaded from SoilGrids https://soilgrids.org (Hengl et al., 2017) and licensed under CC BY 4.0.

Acknowledgments
This research is sponsored by the National Science Foundation (NSF) Office of Polar Programs Grants 1725654 (University of Michigan), 1724868 (Kansas State University), 1724633 (Georgia Tech), and 1724786 (Ohio State University), respectively. The NSF Navigating the New Arctic Program Track-I Grants 2126792, 2126793, 2126797, 2126798 to the same co-authors facilitated this work. V. Ivanov and V. Mazepa acknowledge the support from project RUB1-7032-EK-11 funded by the U.S. Civilian Research & Development Foundation. V. Mazepa acknowledges the partial support from Grant RFBR-19-05-00756 from the Russian Foundation for Basic Research. V. Valdayskikh was supported by the state task of the Ministry of Education and Science of the Russian Federation, project no. FEUZ 2023-0019. The team is highly grateful for the design of field monitoring stations to Yuriy Trubnikov. The field support by Vyacheslav Osokin, Grigoriy Popov, and Andrey Baryshnikov is acknowledged. The team also appreciates the development of the UQ Toolkit (UQTk) from the Uncertainty Quantification group in Sandia National Laboratories. Sandia National Laboratories is a multimission laboratory managed and operated by National Technology and Engineering Solutions of Sandia, LLC., a wholly owned subsidiary of Honeywell International, Inc., for the U. S. Department of Energy's National Nuclear Security Administration under contract DE-NA-0003525. We acknowledge the World Climate Research Programme, which, through its Working Group on Coupled Modelling, coordinated and promoted CMIP6. We thank the climate modeling groups for producing and making available their model output, the Earth System Grid Federation (ESGF) for archiving the data and providing access, and the multiple funding agencies who support CMIP6 and ESGF. The authors also thank the three anonymous reviewers for their valuable comments that improved this manuscript.

References

Apogee Instruments. (2018). *SI-400 infrared radiometer owner's manual*. Apogee Instruments, Inc.
Babacan, S. D., Molina, R., & Katsaggelos, A. K. (2009). Bayesian compressive sensing using Laplace priors. *IEEE Transactions on Image Processing*, *19*(1), 53–63. https://doi.org/10.1109/tip.2009.2032894
Berveiller, M., Sudret, B., & Lemaire, M. (2006). Stochastic finite element: A non intrusive approach by regression. *European Journal of Computational Mechanics/Revue Européenne de Mécanique Numérique*, *15*(1–3), 81–92. https://doi.org/10.3166/remn.15.81-92
Biskaborn, B. K., Smith, S. L., Noetzli, J., Matthes, H., Vieira, G., Streletskiy, D. A., et al. (2019). Permafrost is warming at a global scale. *Nature Communications*, *10*(1), 264. https://doi.org/10.1038/s41467-018-08240-4
Blatman, G., & Sudret, B. (2008). Sparse polynomial chaos expansions and adaptive stochastic finite elements using a regression approach. *Comptes Rendus Mecanique*, *336*(6), 518–523. https://doi.org/10.1016/j.crme.2008.02.013
Blatman, G., & Sudret, B. (2011). Adaptive sparse polynomial chaos expansion based on least angle regression. *Journal of Computational Physics*, *230*(6), 2345–2367. https://doi.org/10.1016/j.jcp.2010.12.021
Brooks, R. H., & Corey, A. T. (1966). Properties of porous media affecting fluid flow. *Journal of the Irrigation and Drainage Division*, *92*(2), 61–88. https://doi.org/10.1061/jrcea4.0000425
Brown, J., Hinkel, K. M., & Nelson, F. E. (2000). The circumpolar active layer monitoring (CALM) program: Research designs and initial results. *Polar Geography*, *24*(3), 166–258. https://doi.org/10.1080/10889370009377698
Campbell Scientific. (2016). *Model HFP01 soil heat flux plate instruction manual. Revision 10/16*. Campbell Scientific, Inc.
Campbell Scientific. (2018). *CS650 and CS655 water content reflectometers instruction manual. Revision 04/18*. Campbell Scientific, Inc.
Cleary, E., Garbuno-Inigo, A., Lan, S., Schneider, T., & Stuart, A. M. (2021). Calibrate, emulate, sample. *Journal of Computational Physics*, *424*, 109716. https://doi.org/10.1016/j.jcp.2020.109716
Cobos, D. R., & Baker, J. M. (2003). In situ measurement of soil heat flux with the gradient method. *Vadose Zone Journal*, *2*(4), 589–594. https://doi.org/10.2136/vzj2003.5890
Cranmer, K., Brehmer, J., & Louppe, G. (2020). The Frontier of simulation-based inference. *Proceedings of the National Academy of Sciences*, *117*(48), 30055–30062. https://doi.org/10.1073/pnas.1912789117
Danabasoglu, G., Lamarque, J. F., Bacmeister, J., Bailey, D. A., DuVivier, A. K., Edwards, J., et al., (2020). The Community Earth System Model Version 2 (CESM2). *Journal of Advances in Modeling Earth Systems*, *12*(2), e2019MS001916. https://doi.org/10.1029/2019ms001916
Debusschere, B., Sargsyan, K., Safta, C., & Chowdhary, K. (2016). Uncertainty quantification toolkit (UQTk). In R. Ghanem, D. Higdon, & H. Owhadi (Eds.), *Handbook of uncertainty quantification* (pp. 1–21). Springer International Publishing. https://doi.org/10.1007/978-3-319-11259-6_56-1
Debusschere, B. J., Najm, H. N., Pébay, P. P., Knio, O. M., Ghanem, R. G., & Le Maıˆtre, O. P. (2004). Numerical challenges in the use of polynomial chaos representations for stochastic processes. *SIAM Journal on Scientific Computing*, *26*(2), 698–719. https://doi.org/10.1137/s1064827503427741
Decker, M., Brunke, M. A., Wang, Z., Sakaguchi, K., Zeng, X., & Bosilovich, M. G. (2012). Evaluation of the reanalysis products from GSFC, NCEP, and ECMWF using flux tower observations. *Journal of Climate*, *25*(6), 1916–1944. https://doi.org/10.1175/jcli-d-11-00004.1
Dong, D., Fang, P., Bock, Y., Webb, F., Prawirodirdjo, L., Kedar, S., & Jamason, P. (2006). Spatiotemporal filtering using principal component analysis and Karhunen-Loeve expansion approaches for regional GPS network analysis. *Journal of Geophysical Research*, *111*(B3), B03405. https://doi.org/10.1029/2005jb003806
Dwelle, M. C., Kim, J., Sargsyan, K., & Ivanov, V. Y. (2019). Streamflow, stomata, and soil pits: Sources of inference for complex models with fast, robust uncertainty quantification. *Advances in Water Resources*, *125*, 13–31. https://doi.org/10.1016/j.advwatres.2019.01.002
Ellison, A. M. (2004). Bayesian inference in ecology. *Ecology Letters*, *7*(6), 509–520. https://doi.org/10.1111/j.1461-0248.2004.00603.x
El Sharif, H., Zhou, W., Ivanov, V., Sheshukov, A., Mazepa, V., & Wang, J. (2019). Surface energy budgets of arctic tundra during growing season. *Journal of Geophysical Research: Atmospheres*, *124*(13), 6999–7017. https://doi.org/10.1029/2019jd030650
Eyring, V., Bony, S., Meehl, G. A., Senior, C. A., Stevens, B., Stouffer, R. J., & Taylor, K. E. (2016). Overview of the Coupled Model Intercomparison Project Phase 6 (CMIP6) experimental design and organization. *Geoscientific Model Development*, *9*(5), 1937–1958. https://doi.org/10.5194/gmd-9-1937-2016
Farouki, O. T. (1981). Thermal properties of soils.
Fitzmaurice, J., Wang, J., & Bras, R. L. (2004). Sensible heat flux estimated from one-level air temperature near the land surface. *Geophysical Research Letters*, *31*(7), L07102. https://doi.org/10.1029/2003gl018452
Fuchs, M., & Tanner, C. B. (1968a). Calibration and field test of soil heat flux plates. *Soil Science Society of America Journal*, *32*(3), 326–328. https://doi.org/10.2136/sssaj1968.03615995003200030021x
Fuchs, M., & Tanner, C. B. (1968b). Surface temperature measurements of bare soils. *Journal of Applied Meteorology*, *7*(2), 303–305. https://doi.org/10.1175/1520-0450(1968)007<0303:Stmobs>2.0.Co;2
Gao, Z., Horton, R., & Liu, H. P. (2010). Impact of wave phase difference between soil surface heat flux and soil surface temperature on soil surface energy balance closure. *Journal of Geophysical Research*, *115*(D16), D16112. https://doi.org/10.1029/2009jd013278
Garnello, A., Marchenko, S., Nicolsky, D., Romanovsky, V., Ledman, J., Celis, G., et al. (2021). Projecting permafrost thaw of sub-arctic tundra with a thermodynamic model calibrated to site measurements. *Journal of Geophysical Research: Biogeosciences*, *126*(6), e2020JG006218. https://doi.org/10.1029/2020jg006218
Ghanem, R., Higdon, D., & Owhadi, H. (2017). *Handbook of uncertainty quantification*. Springer.
Groenke, B., Langer, M., Nitzbon, J., Westermann, S., Gallego, G., & Boike, J. (2022). Investigating the thermal state of permafrost with Bayesian inverse modeling of heat transfer. *EGUsphere*, *2022*, 1–44.
Haario, H., Saksman, E., & Tamminen, J. (2001). *An adaptive Metropolis algorithm* (pp. 223–242). Bernoulli.
Halliwell, D. H., & Rouse, W. R. (1987). Soil heat flux in permafrost: Characteristics and accuracy of measurement. *Journal of Climatology*, *7*(6), 571–584. https://doi.org/10.1002/joc.3370070605
Harlan, R. L. (1973). Analysis of coupled heat-fluid transport in partially frozen soil. *Water Resources Research*, *9*(5), 1314–1323. https://doi.org/10.1029/WR009i005p01314
Harp, D. R., Atchley, A. L., Painter, S. L., Coon, E. T., Wilson, C. J., Romanovsky, V. E., & Rowland, J. C. (2016). Effect of soil property uncertainties on permafrost thaw projections: A calibration-constrained analysis. *The Cryosphere*, *10*(1), 341–358. https://doi.org/10.5194/tc-10-341-2016
Hastings, W. K. (1970). Monte Carlo sampling methods using Markov chains and their applications. *Biometrika*, *57*(1), 97–109. https://doi.org/10.1093/biomet/57.1.97

Hengl, T., Mendes de Jesus, J., Heuvelink, G. B., Ruiperez Gonzalez, M., Kilibarda, M., Blagotic, A., et al. (2017). SoilGrids250m: Global gridded soil information based on machine learning. *PLoS One*, *12*(2), e0169748. https://doi.org/10.1371/journal.pone.0169748

Hersbach, H., Bell, B., Berrisford, P., Hirahara, S., Horányi, A., Muñoz-Sabater, J., et al. (2020). The ERA5 global reanalysis. *Quarterly Journal of the Royal Meteorological Society*, *146*(730), 1999–2049. https://doi.org/10.1002/qj.3803

Heusinkveld, B. G., Jacobs, A., Holtslag, A., & Berkowicz, S. (2004). Surface energy balance closure in an arid region: Role of soil heat flux. *Agricultural and Forest Meteorology*, *122*(1–2), 21–37. https://doi.org/10.1016/j.agrformet.2003.09.005

Hinkel, K. M., Paetzold, F., Nelson, F. E., & Bockheim, J. G. (2001). Patterns of soil temperature and moisture in the active layer and upper permafrost at Barrow, Alaska: 1993–1999. *Global and Planetary Change*, *29*(3–4), 293–309. https://doi.org/10.1016/s0921-8181(01)00096-0

Hinzman, L. D., Kane, D. L., Gieck, R. E., & Everett, K. R. (1991). Hydrologic and thermal properties of the active layer in the Alaskan Arctic. *Cold Regions Science and Technology*, *19*(2), 95–110. https://doi.org/10.1016/0165-232x(91)90001-w

Hjort, J., Streletskiy, D., Doré, G., Wu, Q., Bjella, K., & Luoto, M. (2022). Impacts of permafrost degradation on infrastructure. *Nature Reviews Earth & Environment*, *3*(1), 24–38. https://doi.org/10.1038/s43017-021-00247-8

Horton, R., & Wierenga, P. J. (1983). Estimating the soil heat flux from observations of soil temperature near the surface. *Soil Science Society of America Journal*, *47*(1), 14–20. https://doi.org/10.2136/sssaj1983.03615995004700010003x

Hou, Z., & Rubin, Y. (2005). On minimum relative entropy concepts and prior compatibility issues in vadose zone inverse and forward modeling. *Water Resources Research*, *41*(12), W12425. https://doi.org/10.1029/2005wr004082

Ivanov, V. Y., Xu, D., Dwelle, M. C., Sargsyan, K., Wright, D. B., Katopodes, N., et al. (2021). Breaking down the computational barriers to real-time urban flood forecasting. *Geophysical Research Letters*, *48*(20), e2021GL093585. https://doi.org/10.1029/2021gl093585

Johansen, O. (1977). Thermal conductivity of soils.

Jones, S. B., Wraith, J. M., & Or, D. (2002). Time domain reflectometry measurement principles and applications. *Hydrological Processes*, *16*(1), 141–153. https://doi.org/10.1002/hyp.513

Kane, D. L., Hinzman, L. D., Benson, C. S., & Everett, K. R. (1989). Hydrology of Imnavait Creek, an arctic watershed. *Ecography*, *12*(3), 262–269. https://doi.org/10.1111/j.1600-0587.1989.tb00845.x

Karhunen, K. (1947). *Ueber lineare methoden in der Wahrscheinlichkeitsrechnung*. Soumalainen Tiedeakatemia.

Kimball, B. A., Jackson, R. D., Nakayama, F. S., Idso, S. B., & Reginato, R. J. (1976). Soil-heat flux determination: Temperature gradient method with computed thermal conductivities. *Soil Science Society of America Journal*, *40*(1), 25–28. https://doi.org/10.2136/sssaj1976.03615995004000010011x

Koopmans, R. W. R., & Miller, R. (1966). Soil freezing and soil water characteristic curves. *Soil Science Society of America Journal*, *30*(6), 680–685. https://doi.org/10.2136/sssaj1966.03615995003000060011x

Lawrence, D. M., & Slater, A. G. (2007). Incorporating organic soil into a global climate model. *Climate Dynamics*, *30*(2–3), 145–160. https://doi.org/10.1007/s00382-007-0278-1

Le Maître, O., & Knio, O. M. (2010). *Spectral methods for uncertainty quantification: With applications to computational fluid dynamics*. Springer Science & Business Media.

Leuning, R., van Gorsel, E., Massman, W. J., & Isaac, P. R. (2012). Reflections on the surface energy imbalance problem. *Agricultural and Forest Meteorology*, *156*, 65–74. https://doi.org/10.1016/j.agrformet.2011.12.002

Lindsay, R., Wensnahan, M., Schweiger, A., & Zhang, J. (2014). Evaluation of seven different atmospheric reanalysis products in the Arctic. *Journal of Climate*, *27*(7), 2588–2606. https://doi.org/10.1175/jcli-d-13-00014.1

Loève, M. (1948). *Fonctions aleatoires du second ordre, supplement to P.* Lévy, Processus Stochastiques et Mouvement Brownien. Gauthier-Villars.

Lunardini, V. J. (1981). *Heat transfer in cold climates*. Van Nostrand Reinhold Company.

Malinverno, A. (2002). Parsimonious Bayesian Markov chain Monte Carlo inversion in a nonlinear geophysical problem. *Geophysical Journal International*, *151*(3), 675–688. https://doi.org/10.1046/j.1365-246X.2002.01847.x

Malkova, G., Drozdov, D., Vasiliev, A., Gravis, A., Kraev, G., Korostelev, Y., et al. (2022). Spatial and temporal variability of permafrost in the western part of the Russian Arctic. *Energies*, *15*(7), 2311. https://doi.org/10.3390/en15072311

Matzner, E., & Borken, W. (2008). Do freeze-thaw events enhance C and N losses from soils of different ecosystems? A review. *European Journal of Soil Science*, *59*(2), 274–284. https://doi.org/10.1111/j.1365-2389.2007.00992.x

Melnikov, E., Leibman, M., Moskalenko, N., & Vasiliev, A. (2004). Active-layer monitoring in the cryolithozone of west Siberia. *Polar Geography*, *28*(4), 267–285. https://doi.org/10.1080/789610206

Miller, R. D. (1980). 11 - Freezing phenomena in soils. In D. Hillel (Ed.), *Applications of soil physics* (pp. 254–299). Academic Press. https://doi.org/10.1016/B978-0-12-348580-9.50016-X

Mu, S., & Ladanyi, B. (1987). Modeling of coupled heat, moisture and stress-field in freezing soil. *Cold Regions Science and Technology*, *14*(3), 237–246. https://doi.org/10.1016/0165-232x(87)90016-4

Muñoz Sabater, J. (2019). ERA5-Land hourly data from 1950 to present. Copernicus Climate Change Service (C3S) Climate Data Store (CDS). https://doi.org/10.24381/CDS.E2161BAC

Muñoz-Sabater, J., Dutra, E., Agustí-Panareda, A., Albergel, C., Arduini, G., Balsamo, G., et al. (2021). ERA5-Land: A state-of-the-art global reanalysis dataset for land applications. *Earth System Science Data*, *13*(9), 4349–4383. https://doi.org/10.5194/essd-13-4349-2021

Nicolsky, D., Romanovsky, V., & Panteleev, G. (2009). Estimation of soil thermal properties using in-situ temperature measurements in the active layer and permafrost. *Cold Regions Science and Technology*, *55*(1), 120–129. https://doi.org/10.1016/j.coldregions.2008.03.003

Nicolsky, D. J., & Romanovsky, V. E. (2018). Modeling long-term permafrost degradation. *Journal of Geophysical Research: Earth Surface*, *123*(8), 1756–1771. https://doi.org/10.1029/2018jf004655

Ochsner, T. E., & Baker, J. M. (2008). In situ monitoring of soil thermal properties and heat flux during freezing and thawing. *Soil Science Society of America Journal*, *72*(4), 1025–1032. https://doi.org/10.2136/sssaj2007.0283

Ochsner, T. E., Sauer, T. J., & Horton, R. (2006). Field tests of the soil heat flux plate method and some alternatives. *Agronomy Journal*, *98*(4), 1005–1014. https://doi.org/10.2134/agronj2005.0249

Painter, S. L., Coon, E. T., Atchley, A. L., Berndt, M., Garimella, R., Moulton, J. D., et al. (2016). Integrated surface/subsurface permafrost thermal hydrology: Model formulation and proof-of-concept simulations. *Water Resources Research*, *52*(8), 6062–6077. https://doi.org/10.1002/2015wr018427

Painter, S. L., & Karra, S. (2014). Constitutive model for unfrozen water content in subfreezing unsaturated soils. *Vadose Zone Journal*, *13*(4), 8. https://doi.org/10.2136/vzj2013.04.0071

Painter, S. L., Moulton, J. D., & Wilson, C. J. (2012). Modeling challenges for predicting hydrologic response to degrading permafrost. *Hydrogeology Journal*, *21*(1), 221–224. https://doi.org/10.1007/s10040-012-0917-4

Rundle, J. B., Klein, W., Tiampo, K., & Gross, S. (2000). Linear pattern dynamics in nonlinear threshold systems. *Physical Review E*, *61*(3), 2418–2431. https://doi.org/10.1103/physreve.61.2418

Sargsyan, K., Najm, H., & Ghanem, R. (2015). On the statistical calibration of physical models. *International Journal of Chemical Kinetics*, *47*(4), 246–276. https://doi.org/10.1002/kin.20906

Sargsyan, K., Safta, C., Najm, H. N., Debusschere, B. J., Ricciuto, D., & Thornton, P. (2014). Dimensionality reduction for complex models via Bayesian compressive sensing. *International Journal for Uncertainty Quantification*, *4*(1), 63–93. https://doi.org/10.1615/int.j.uncertaintyquantification.2013006821

Sheshukov, A. Y., & Egorov, A. G. (2002). Frozen barrier evolution in saturated porous media. *Advances in Water Resources*, *25*(6), 591–599. https://doi.org/10.1016/s0309-1708(02)00033-7

Sheshukov, A. Y., & Nieber, J. L. (2011). One-dimensional freezing of nonheaving unsaturated soils: Model formulation and similarity solution. *Water Resources Research*, *47*(11), W11519. https://doi.org/10.1029/2011wr010512

Smolyak, S. A. (1963). *Quadrature and interpolation formulas for tensor products of certain classes of functions*. Doklady Akademii Nauk.

Sraj, I., Mandli, K. T., Knio, O. M., Dawson, C. N., & Hoteit, I. (2014). Uncertainty quantification and inference of Manning's friction coefficients using DART buoy data during the Tōhoku tsunami. *Ocean Modelling*, *83*, 82–97. https://doi.org/10.1016/j.ocemod.2014.09.001

Tarantola, A. (2005). *Inverse problem theory and methods for model parameter estimation*. SIAM.

Taylor, G. S., & Luthin, J. N. (1978). A model for coupled heat and moisture transfer during soil freezing. *Canadian Geotechnical Journal*, *15*(4), 548–555. https://doi.org/10.1139/t78-058

Tiampo, K., Rundle, J., Klein, W., Ben-Zion, Y., & McGinnis, S. (2004). Using eigenpattern analysis to constrain seasonal signals in Southern California. *Computational Earthquake Science Part*, *I*(9–10), 1991–2003. https://doi.org/10.1007/s00024-004-2545-y

Tubini, N., Gruber, S., & Rigon, R. (2021). A method for solving heat transfer with phase change in ice or soil that allows for large time steps while guaranteeing energy conservation. *The Cryosphere*, *15*(6), 2541–2568. https://doi.org/10.5194/tc-15-2541-2021

Vasiliev, A., Leibman, M., & Moskalenko, N. (2008). Active layer monitoring in West Siberia under the CALM II program. In *Proc. Ninth Int. Conf. Permafrost*.

Walvoord, M. A., & Kurylyk, B. L. (2016). Hydrologic impacts of thawing permafrost—A review. *Vadose Zone Journal*, *15*(6), 1–20. https://doi.org/10.2136/vzj2016.01.0010

Wang, J., & Bras, R. L. (1998). A new method for estimation of sensible heat flux from air temperature. *Water Resources Research*, *34*(9), 2281–2288. https://doi.org/10.1029/98wr01698

Wang, J., & Bras, R. L. (1999). Ground heat flux estimated from surface soil temperature. *Journal of Hydrology*, *216*(3–4), 214–226. https://doi.org/10.1016/S0022-1694(99)00008-6

Wang, Z.-H., & Bou-Zeid, E. (2012). A novel approach for the estimation of soil ground heat flux. *Agricultural and Forest Meteorology*, *154–155*, 214–221. https://doi.org/10.1016/j.agrformet.2011.12.001

Westermann, S., Ingeman-Nielsen, T., Scheer, J., Aalstad, K., Aga, J., Chaudhary, N., et al. (2023). The CryoGrid community model (version 1.0)–a multi-physics toolbox for climate-driven simulations in the terrestrial cryosphere. *Geoscientific Model Development*, *16*(9), 2607–2647. https://doi.org/10.5194/gmd-16-2607-2023

Westermann, S., Langer, M., Boike, J., Heikenfeld, M., Peter, M., Etzelmüller, B., & Krinner, G. (2016). Simulating the thermal regime and thaw processes of ice-rich permafrost ground with the land-surface model CryoGrid 3. *Geoscientific Model Development*, *9*(2), 523–546. https://doi.org/10.5194/gmd-9-523-2016

Wu, B., Oncley, S. P., Yuan, H., & Chen, F. (2020). Ground heat flux determination based on near-surface soil hydro-thermodynamics. *Journal of Hydrology*, *591*, 125578. https://doi.org/10.1016/j.jhydrol.2020.125578

Zhang, X., Sun, S. F., & Xue, Y. K. (2007). Development and testing of a frozen soil parameterization for cold region studies. *Journal of Hydrometeorology*, *8*(4), 690–701. https://doi.org/10.1175/Jhm605.1

Zhou, W., & Ivanov, V. (2023). *Soil temperature, moisture, and ground heat flux measurements at LPTEG-TREES-1 site, 2019/07/01-2019/09/09*. Zenodo. https://doi.org/10.5281/zenodo.7600654